



HAL
open science

Coupling grid nanoindentation and surface chemical analysis to infer the mechanical properties of shale mineral phases

Jianting Du, Andrew Whittle, Liming Hu, Thibaut Divoux, Jay Meegoda

► **To cite this version:**

Jianting Du, Andrew Whittle, Liming Hu, Thibaut Divoux, Jay Meegoda. Coupling grid nanoindentation and surface chemical analysis to infer the mechanical properties of shale mineral phases. *Engineering Geology*, 2023, 325, pp.107304. 10.1016/j.enggeo.2023.107304 . hal-04251956

HAL Id: hal-04251956

<https://hal.science/hal-04251956>

Submitted on 20 Oct 2023

HAL is a multi-disciplinary open access archive for the deposit and dissemination of scientific research documents, whether they are published or not. The documents may come from teaching and research institutions in France or abroad, or from public or private research centers.

L'archive ouverte pluridisciplinaire **HAL**, est destinée au dépôt et à la diffusion de documents scientifiques de niveau recherche, publiés ou non, émanant des établissements d'enseignement et de recherche français ou étrangers, des laboratoires publics ou privés.

1 **Coupling grid nanoindentation and surface chemical analysis to infer**
2 **the mechanical properties of shale mineral phases**

3 Jianting Du^a, Andrew J. Whittle^b, Liming Hu^c, Thibaut Divoux^{d, e}, Jay N. Meegoda^{c, f}

4 ^aState Key Laboratory of Internet of Things for Smart City and Department of Civil and Environmental
5 Engineering, University of Macau, Macau, China

6 ^bDepartment of Civil and Environmental Engineering, Massachusetts Institute of Technology, Cambridge,
7 MA 02139, USA

8 ^cState Key Laboratory of Hydro-Science and Engineering, Tsinghua University, Beijing 100084, China

9 ^dMultiScale Material Science for Energy and Environment, UMI 3466, CNRS-MIT, Cambridge, MA 02139,
10 USA

11 ^eENSL, CNRS, Laboratoire de Physique, F-69342 Lyon, France

12 ^fDepartment of Civil and Environmental Engineering, New Jersey Institute of Technology, NJ 07102, USA

13

14 **Highlights:**

- 15 • A protocol was developed for coupling analysis of grid nanoindentation and local
16 mineralogy.
- 17 • Quartz and illite phases can be subdivided between intact particles and nano-porous
18 aggregates.
- 19 • Self-consistent modeling provides a basis for upscaling properties from intact particles
20 to mineral aggregates.

21

22

23 **Abstract**

24 Shale is a low-permeability, multi-phase, and multi-scale composite material with intrinsic
25 heterogeneity in micro-texture and mineralogical composition. In this paper, relationships
26 between the microscale texture and constituent phases of shale were investigated using the
27 SEM (scanning electron microscopy)/BSE (backscatter electron imaging)-EDS (energy-
28 dispersive x-ray spectroscopy) methods, and grid nanoindentation experiments. The
29 mechanical properties of the constituent phases of the carbonate-rich Longmaxi shale
30 samples were extracted based on the spatial distribution of mineral phases and the
31 indentation interaction volume. The effects of particle size on the interpreted mechanical
32 properties were analyzed and a characteristic length scale was determined based on a
33 probabilistic analysis. The identified characteristic length for extracting the mechanical
34 properties of constituent mineral phases from the grid nanoindentation technique is about
35 5.8 - 11.7 μm , i.e., up to 10 times greater than that proposed in prior research. A multi-
36 scale mechanical model was established with considerations of a self-consistent scheme
37 for granular morphology to link the microscopic characteristics with the multi-scale
38 mechanical properties of shales. The modeling results showed that the stiffness and the
39 strength of the homogenized nano-porous illite/quartz aggregates in Longmaxi shale can
40 be assessed from the nano-scale mechanical properties of the mineral phases and the nano-
41 scale porosity. This study paves the way to accessing the mechanical properties of the
42 constituent phases of composite materials based on the properties of their building blocks
43 and provides extensive insights into their complex mechanical behavior, representing a
44 major step towards developing reliable multi-scale models for engineering applications.

45

46 **Keywords:** Shale; grid nanoindentation; in-situ mineral identification; mechanical
47 properties of the constituent phases; multi-scale mechanical model

48

49 **1 Introduction**

50 Shales are fine-grained sedimentary rocks mainly composed of highly consolidated
51 aggregates of clay minerals (phyllosilicates), silt-sized particles of other common soil
52 minerals (e.g., tectosilicates such as quartz and feldspar, and carbonates), and organic
53 matter. Shale formations play important roles in applications such as the geological
54 containment of radioactive waste (Neuzil 2013), extraction of natural gas (Du et al. 2018),
55 and sequestration of carbon dioxide (Boosari et al. 2015; Elliot and Celia 2012; Middleton
56 et al. 2014). The engineering challenges associated with these applications require an in-
57 depth evaluation of the mechanical and mineralogical properties of shales.

58 Shale is a porous, multi-phase, and multi-scale composite material with intrinsic
59 heterogeneity in microtexture, mineralogy, and mechanical properties, and hence, the
60 accurate measurement of its bulk mechanical properties or interpretation from its
61 constituent phases continues to be a formidable challenge for the geomechanics
62 community. The development of nanoindentation methods, first proposed by Oliver and
63 Pharr (1992, 2004), makes it possible to obtain the local mechanical properties of
64 composite material at micro- and nano-scales. In that framework, the grid-indentation
65 approach can probe constituents' mechanical properties in highly heterogeneous and multi-
66 phase materials, such as shales and concretes (Bobko and Ulm 2008; Constantinides et al.
67 2006; Ulm and Abousleiman 2006; Ulm et al. 2007). Furthermore, statistical deconvolution
68 through a multivariate Gaussian Mixture Model (GMM) can be applied to identify the local
69 mechanical properties of individual constituent phases (Liu et al. 2018; Liu et al. 2021;
70 Luo et al. 2021; Luo et al. 2020; Wu et al. 2020; Xu et al. 2020). However, this prior work
71 has applied statistical analyses of the mechanical data without direct reference to the local
72 mineralogy and hence, phases of different mineralogy but similar mechanical response, as
73 well as their mixtures, may manifest as a single microstructural component potentially
74 resulting in bias of the statistical deconvolution analysis. Although further efforts have

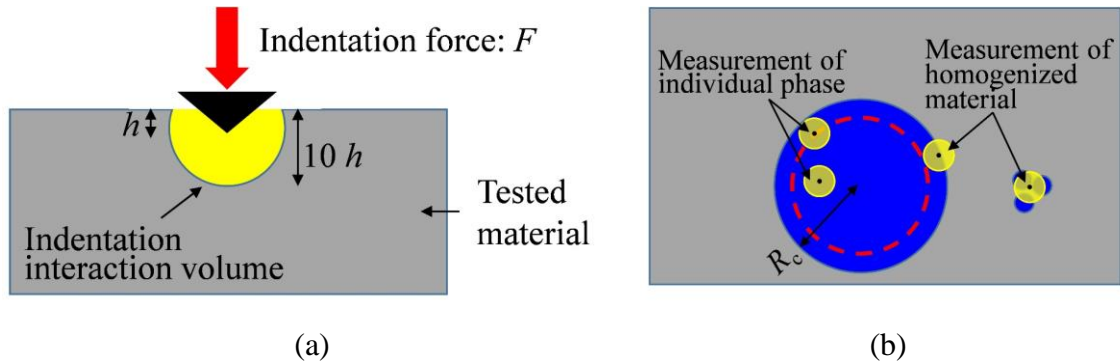
75 been made to reflect the mineralogy by using electron probe microanalyzer (EPMA)
76 techniques (Abedi et al. 2016; Deirieh et al. 2012; Mashhadian et al. 2018; Veytskin et al.
77 2017), the direct link between the nanoindentation measurements and local mineralogy to
78 infer mechanical properties of shale mineral phases has not been established to date.

79 Recently, Liu et al. (2022) studied the nano-scale mechanical properties of constituent
80 minerals in shales by combining nanoindentation statistical analyses and SEM-EDS-XRD
81 techniques. The residual impressions of nanoindentation grids were visually checked under
82 SEM/BSE imaging and the local mineralogy under the residual impressions was analyzed
83 using EDS measurements. In this case, the measurements should correspond to mineral
84 phases within the deformed zone, rather than those directly under the indent impression.
85 This is illustrated by considering the stress conditions beneath an indenter (**Fig. 1a**).
86 Elastoplastic deformations can occur within a highly stressed zone beneath the indenter tip
87 contact that is 10 times greater than the indentation depth (Durst et al. 2005; Larsson et al.
88 1996). Moreover, particle size effects and similarities in the mechanical properties of
89 certain mineral phases can result in bias in evaluating nano-scale mechanical properties.

90 In a shale sample, with a broad range of particle sizes, the process zone can either be
91 contained within a single mineral phase or be influenced by particles of distinct constituent
92 phases (and hence, represent local homogenization of the individual phases), as illustrated
93 in **Fig. 1b**. Moreover, the volume fractions of the constituent phases are closely linked to
94 the bulk mechanical properties of shale (Abedi et al. 2016; Kuila et al. 2014). However,
95 the prior studies generally infer volume fractions of minerals from mass fractions using
96 semi-quantitative XRD methods (with average densities reported independently) (Abedi et
97 al. 2016; Chen et al. 2015).

98 In light of these limitations, we have investigated the nano-scale properties of
99 individual shale phases by combining grid nanoindentation data with high-resolution
100 digital mineralogy maps. The particle size distributions of constituent mineral phases are

101 extracted with an edge detection algorithm to better estimate nano-scale mechanical
 102 properties. We show how these nano-scale properties of individual shale phases can be
 103 reliably determined and upscaled to estimate the macro-scale homogeneous mechanical
 104 properties of the composite material.
 105



106 **Fig. 1.** Effects of particle size on indentation measurements. a) Influence zone deformed in an
 107 elastoplastic fashion beneath the indenter tip; b) Particles (blue) with characteristic dimension R_c
 108 embedded in a matrix (grey). Indents at the edge of large particles or impinging on small inclusions will
 109 measure the homogenized response of the two phases.

110

111 2 Materials and Methods

112 2.1 Samples and surface preparation

113 The samples used in this research are from the Silurian Longmaxi Formation in
 114 Sichuan Basin, China. This shale is composed of abundant brittle minerals, mainly
 115 feldspar, mica, quartz, and carbonate (average 56.3%) and displays a relatively high
 116 porosity ranging from 1.2 - 10.8% (Dai et al. 2014). The shale samples do not show any
 117 visible bedding planes. Small cuboidal specimens with dimensions ($2\text{cm} \times 2\text{cm} \times 1\text{cm}$;
 118 Length \times Width \times Thickness) were trimmed from large shale block samples using an
 119 IsoMet 1000 precision saw (Buehler Inc., IL, USA). A total of seven trimmed shale

120 specimens (M1 - M7) were used to enable comparisons across specimens from different
121 locations and target test patches.

122 Two surface preparation methods were investigated in this study. The first method
123 consists of dry-mechanical polishing (using SiC paper with grit size $> 0.25\text{mm}$) and
124 ultrasonication in n-decane solution; while the second involves Argon milling using a
125 cross-section polisher (JEOL Inc., MA, USA) with a maximum accelerating voltage of 6
126 kV (to minimize heat damage). Appendix A summarizes the specification of the procedures
127 of Argon milling.

128 The surface roughness of the polished specimens was measured using an Atomic
129 Force Microscope (AFM) (Oxford Instruments Asylum Research Inc., CA, USA) with a
130 wave mode or ‘tapping’ scan (Simpson et al. 1999). The specimens were characterized by
131 a roughness $R_q = 15\text{ nm}$ and 50 nm for mechanical polishing and Argon milling,
132 respectively. Following prior studies (Bobji and Biswas 1999; Donnelly et al. 2006), which
133 involve indentation depth h such that $h > 3R_q$, experiments in this study were designed with
134 a target penetration depth of 100 nm to 400 nm . **Fig. A2** shows that the polishing method
135 had minimal impact on the engineering properties computed from grid indentation
136 experiments; hence, the data reported in this paper are all based on specimens prepared by
137 the more efficient mechanical polishing method.

138

139 **2.2 Grid Nanoindentation Tests**

140 Indentation measurements were performed on seven mechanically polished
141 specimens (M1 - M7) of carbonate-rich Longmaxi shale using a NanoTest indenter (Anton
142 Paar, Graz, Austria) equipped with a Berkovich tip (half-angle 70.32° and curvature radius
143 of approximately 30 nm). The setup allows applying loads ranging between 0.1 and 500
144 mN with a resolution of $0.04\text{ }\mu\text{N}$. Indentation tests were performed on a square grid ($n^2 =$
145 21×21) with $10\text{ }\mu\text{m}$ separation (total patch area, $A = 0.04\text{ mm}^2$) to avoid interactions

146 between adjacent indents (Ulm and Abousleiman 2006). Each test followed a standard
 147 loading function to a prescribed maximum force of 4.0 mN, resulting in a maximum
 148 indentation depth varying between 100 nm and 400 nm according to the local mineralogy
 149 and particle texture. The load was held constant for 2 mins before unloading (with $|dF/dt|$
 150 = 15 mN/min in both loading and unloading). From each indentation test, two quantities
 151 were computed. First, the hardness, H , is defined as follows:

$$152 \quad H = \frac{F_{\max}}{A_c} \quad (1)$$

153 where F_{\max} is the maximum indentation load, and A_c is the projected contact area. The
 154 contact area function is well-defined for a perfectly sharp Berkovich tip. In practice,
 155 however, the Berkovich indenter exhibits some bluntness, which can significantly affect
 156 the interpretation of results, especially for shallow indentations. Thus, in this study, A_c is
 157 determined by indentation on a material whose mechanical properties are known (e.g.,
 158 fused silica, which has an indentation modulus $M = 72$ GPa). A_c is a function of the contact
 159 depth, h_c :

$$160 \quad A_c = C_1 h_c^2 + C_2 h_c + C_3 h_c^{1/2} + C_4 h_c^{1/4} + \dots \quad (2)$$

$$162 \quad h_c / h_{\max} = 1 - \varepsilon F_{\max} / (S h_{\max}) \quad (3)$$

164 where C_1 is usually determined by the area-to-depth constant of the perfectly sharp indenter
 165 (e.g., for a Berkovich indenter, $C_1 = 24.58$) and $\{C_i\}_{i>1}$ are the factors that attribute to the
 166 bluntness of the indenter. ε is a constant related to the geometry of the indenter, and S is
 167 the contact stiffness, which can be calculated by evaluating the derivative at the maximum
 168 load:

$$169 \quad S = \left. \frac{\delta F}{\delta h} \right|_{h_{\max}} \quad (4)$$

170 Second, Young's modulus, E , of the indented bulk material can be obtained from the
171 unload force-displacement curve:

$$172 \quad E = (1-\nu^2) / \left(\frac{1}{M} - \frac{1-\nu_i^2}{E_i} \right) \quad (5)$$

173 where ν and ν_i are the Poisson's ratio of the test sample and the diamond indenter (0.07),
174 respectively; M is the reduced or indentation modulus, which coincides with the plane
175 stress modulus for rigid indentation of an isotropic material; E_i is Young's Modulus of the
176 diamond indenter (1140 GPa).

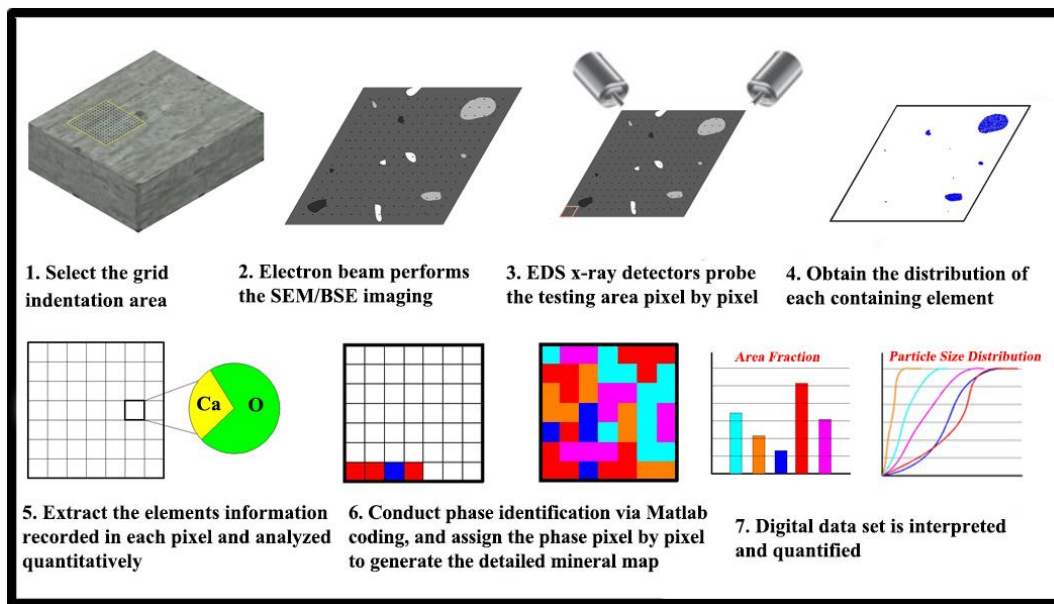
177 Poisson's ratio of shales has been measured and reported in the literature. Typical
178 ranges $\nu = 0.1 - 0.3$ and $0.15 - 0.35$ have been reported in prior studies for Longmaxi shale
179 (Chen et al. 2018; Yang et al. 2016) and Barnett shale (Guo et al. 2013), respectively. Here,
180 we assume $\nu = 0.2$ for interpreting E across all samples. Prior work has demonstrated that
181 the uncertainty on ν has limited influence on the estimation of E (Oliver and Pharr 1992;
182 Zhang et al. 2009).

183

184 **2.3 Method to Interpret Local Mineralogy**

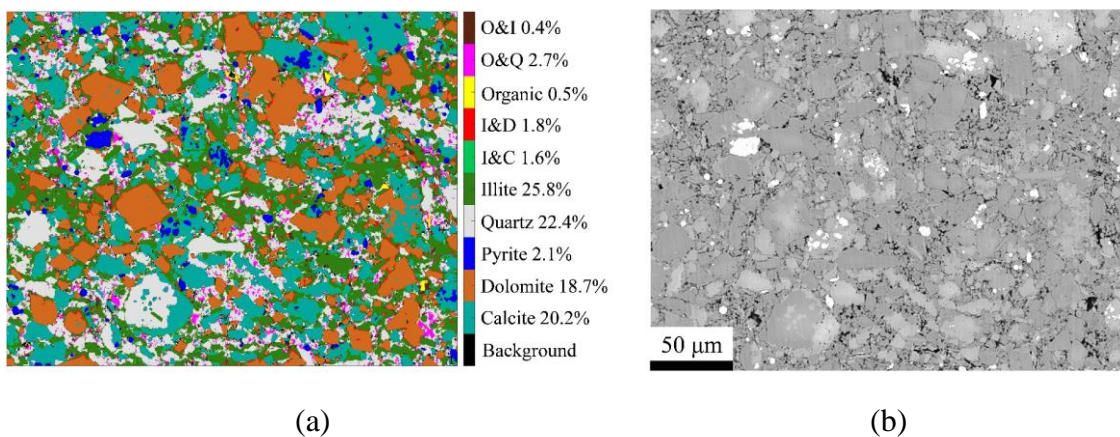
185 The test procedure, illustrated in **Fig. 2**, involves the selection of the area tested by
186 grid nanoindentation using SEM imaging, followed by the insertion of electron backscatter
187 diffraction (EBSD) analyzers to generate the BSE image and EDS map with a resolution
188 of 800×1024 pixels ($0.24 \text{ mm} \times 0.3 \text{ mm}$), each pixel corresponding to $300 \text{ nm} \times 300 \text{ nm}$.
189 The quantitative element information stored in each pixel was then extracted through a
190 Matlab code. After acquiring the distribution of each containing element, the unique
191 elements of each mineral phase are used for mineralogical identification. For instance,
192 silicon, aluminum, and potassium are used to identify illite. If only high-intensity silicon
193 and no other unique elements (i.e., magnesium, iron, sulfur, aluminum, and potassium) are
194 detected in a pixel, this pixel will be identified as the quartz phase. However, if all high-
195 intensity silicon, aluminum, and potassium are detected in a pixel, this pixel will be
196 identified as an illite phase. Carbon and oxygen are not used as unique elements to analyze

197 the mineral phases due to their wide existence in most of the constituent phases in shale.
 198 Based on the elemental chemical composition in each pixel, the in-situ mineralogy can be
 199 uniquely identified pixel by pixel. Finally, a ‘digital mineralogy map’ was obtained that
 200 determines the edges of particles, the area fraction, and the spatial distribution of each
 201 component phase. The results of this approach are illustrated in **Fig. 3**. They closely match
 202 the microstructure observed in the BSE image of the same region, with six pure mineral
 203 phases (illite, quartz, calcite, dolomite, pyrite, and organics) and up to six mixed phases.
 204



205
 206 **Fig. 2.** Procedure for in-situ mineralogical identification.

207



208 **Fig. 3.** a) ‘Digital mineralogy map’ generated by the in-situ mineralogical identification technique and

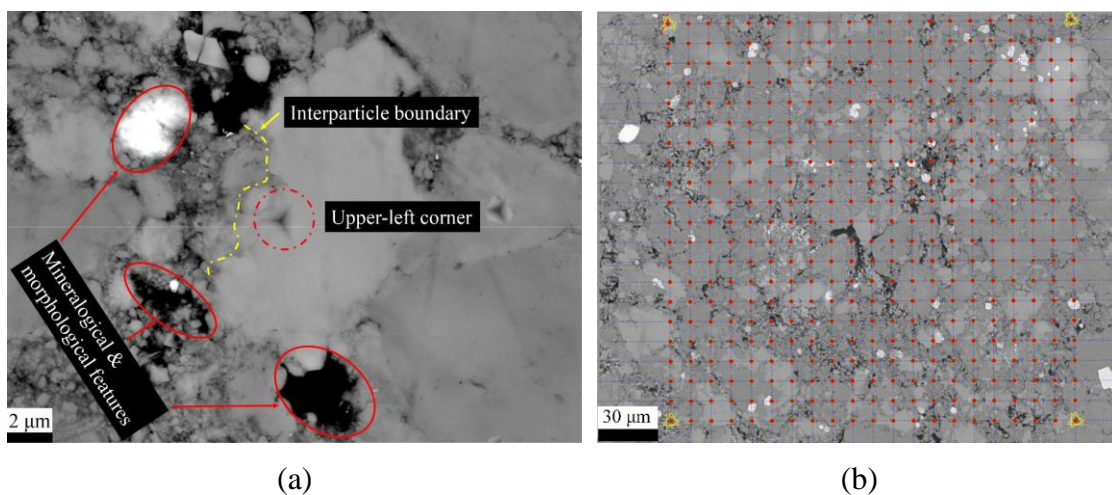
209 b) BSE image of the same region of interest (ROI). The labels ‘C’, ‘D’, ‘Q’, ‘I’, and ‘O’ represent calcite,
210 dolomite, quartz, illite, and organic, respectively. The particles of mineral phases, which appear with
211 different gray scales in the BSE image, agree with the identification results in the ‘digital mineralogy
212 map’.

213

214 2.4 Matching of Mineralogy and Indenter Footprint

215 In order to assign the nano-scale mechanical properties inferred from the
216 nanoindentation grid to their corresponding mineral phases, it is essential to obtain
217 precisely the spatial information of the nanoindentation grid. However, due to the size of
218 each indentation footprint and the lack of contrast between the footprint and the tested shale
219 surface, it is impossible to distinguish individual indents while visualizing the entire
220 nanoindentation grid in the region of interest. Thus, in this study, BSE scanning was used
221 to locate the four corners of the grid (from the indentation footprints) and adjacent key
222 morphological features, as illustrated in **Fig. 4a**. Then, the individual indents were
223 determined assuming a regular pattern for the nanoindentation grid (rows and columns are
224 perpendicular with each other), as illustrated in **Fig. 4b**.

225



226 **Fig. 4.** Determination of nanoindentation grid coordinates. (a) Mineralogical and morphological features
227 in the vicinity of the top-left corner point of the indentation grid observed by high-magnification BSE

228 imaging; (b) indentation grid overlaying the BSE image of the ROI. The grid is positioned assuming a
229 perfectly squared grid based on the knowledge of the corner coordinates.

230

231 The projected area of each indent was calculated according to the measured
232 penetration depth (Eq. 2) and superimposed on the pixel-scale digital mineralogy map (**Fig.**
233 **5**). The constituent mineral phases were assigned to the pixels included in the indentation
234 interaction volume based on the spatial information of the mineral phases in the in-situ
235 ‘digital mineralogy map’ and the coordinates of the indentation grid. The related mineral
236 phase was then classified either as a single constituent phase (> 90% of the pixels display
237 the same mineralogy) or a mixed phase based on the pixel ratio, which defines the number
238 of pixels displaying the same mineralogy in the indentation interaction volume, N_m , to the
239 total number of the pixels included in the interaction volume, N_t , i.e., N_m/N_t . We adopt a
240 conservative rule of thumb, if the proportion of other minor identified constituents is lower
241 than 10%, the measured phase is considered a pure mineral phase (e.g., calcite phase). The
242 measured phase is classified as a mixture phase if two or more phases, each representing
243 more than 10%, are present.

244

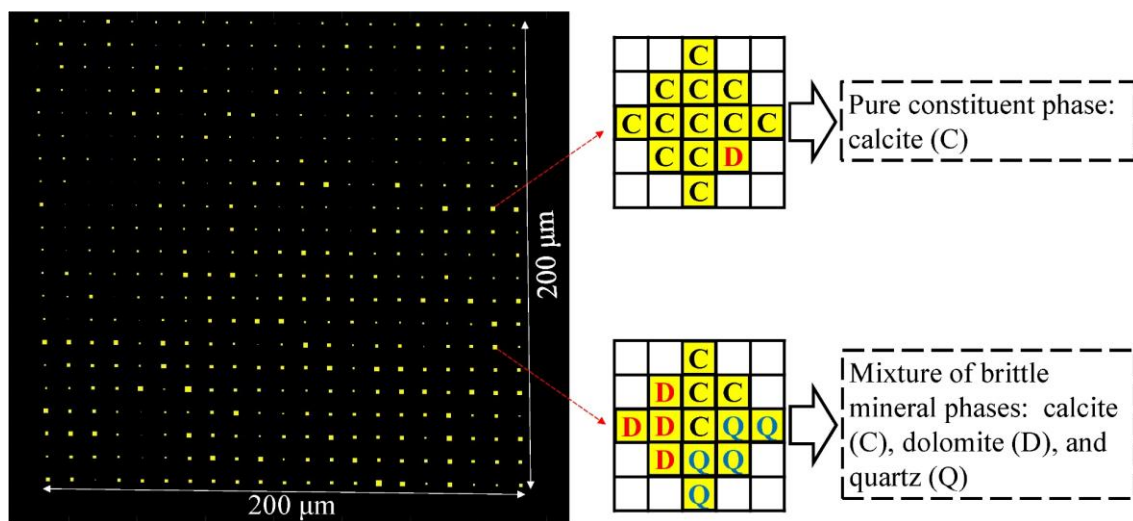


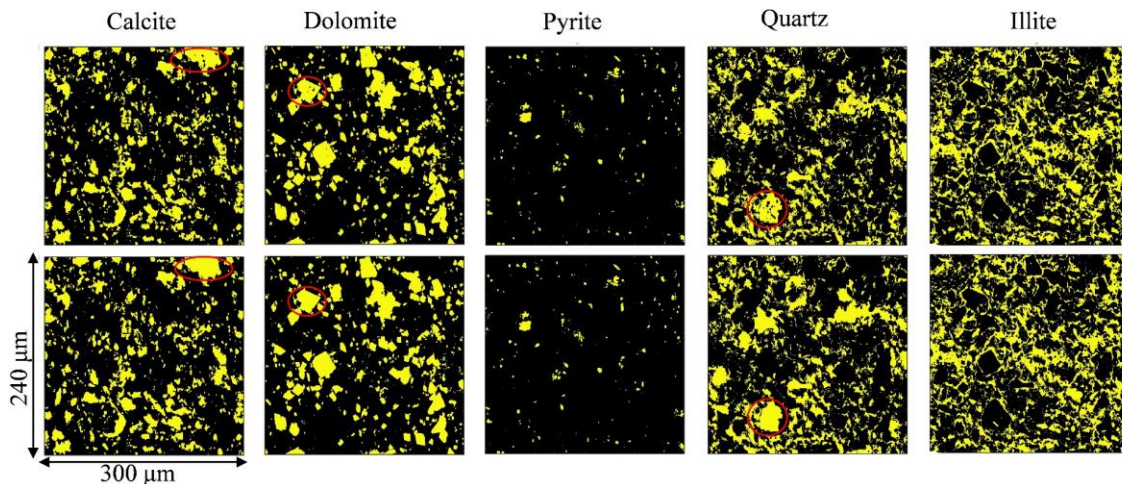
Fig. 5. Mechanical and mineralogical information matching.

247

248 2.5 Particle Size Distribution of mineral phases

249 Particle size distributions of shale mineral phases are quantified by processing the
250 digital mineralogy map (**Fig. 3**). An edge detection algorithm, which has been widely used
251 for quantitative analysis of particle and pore size in a porous medium such as soil and rock
252 (Jiu et al. 2018; Jiu et al. 2020; Wu and Yu 2012; Zhou et al. 2018), is applied using a
253 customized Matlab code. Small holes inside the particles of mineral phases (see, e.g., red
254 circles in **Fig. 6**) are filled first. Then the boundary of each particle is identified by the
255 connection algorithm, which labels connected components in 2D binary image before
256 counting and recording the number of pixels occupied by each particle. Finally, based on
257 the relationship between the actual length and pixel size, the true area of each particle is
258 calculated, which allows us to compute the cumulative distribution of particle area for each
259 mineral phase. It should be noted that particles or pores with a size smaller than the pixel
260 size ($300 \text{ nm} \times 300 \text{ nm}$) cannot be detected in this analysis.

261



262

263 **Fig. 6.** Procedures for particle size calculation. The first row shows the distribution map of each mineral
264 phase identified by the in-situ mineralogical identification. Small holes inside each isolated particle (see
265 red circled) are filled before counting and recording the number of pixels occupied by each particle (the
266 second row).

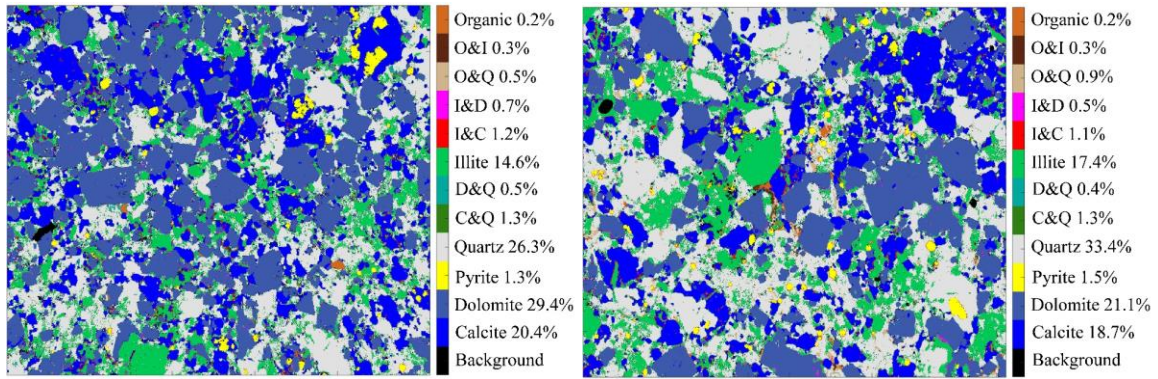
267

268 **3 Results**

269 **3.1 Mineralogy and Particle Size Distribution**

270 **Fig. 7** shows two high-resolution digital maps of the mineralogy of Longmaxi shale
271 samples (specimens M3 and M4). These results highlight the complex microstructure of
272 shale, which is characterized principally by five mineral phases, i.e., quartz, calcite,
273 dolomite, illite, and pyrite. These phases constitute about 90% of the surface area, among
274 which pyrite and organics display much smaller fractions. Since each pixel in the digital
275 mineralogy map corresponds to an area of $300 \text{ nm} \times 300 \text{ nm}$, up to 6 mixed phases (with a
276 total area fraction of about 5.5%) were detected at the junctions between different mineral
277 phases. These mixed phases were further classified into three categories: 1) brittle mixtures
278 (any combination of calcite, C, dolomite, D, quartz, Q and pyrite, P); 2) ductile mixtures
279 (combination of organic, O, and illite, I); and 3) composite mixtures (combinations of
280 minerals from both brittle and ductile groups). Specifically, the C&Q and D&Q phases
281 were classified as brittle mixtures, whereas the I&O phase was classified as a ductile
282 mixture. Finally, the I&C, I&D, and I&Q phases are classified as composite mixtures.
283 **Table 1** summarizes the area fractions of the pure and mixed phases (found in 8 regions of
284 interest) for the seven specimens of the carbonate-rich Longmaxi shale. The measured area
285 fraction of each mineral phase exhibited a relatively small standard deviation (of about 0.5
286 ~ 5%) over the ROI ($240 \text{ } \mu\text{m} \times 300 \text{ } \mu\text{m}$).

287



(a)

(b)

288 **Fig. 7.** Quantitative mineralogical maps (240 $\mu\text{m} \times 300 \mu\text{m}$) for samples M3 (a) and M4 (b) obtained
 289 by in-situ mineralogical identification.

290 **Table 1**

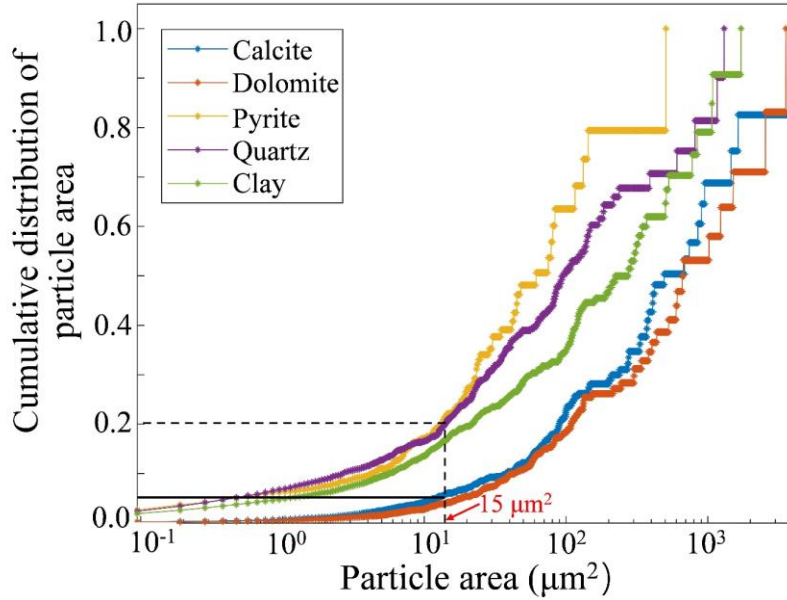
291 Area fractions of mineral phases in carbonate-rich Longmaxi shale.

Sample ID	Calcite (%)	Dolomite (%)	Pyrite (%)	Quartz (%)	Illite (%)	Organic (%)	C&Q (%)	D&Q (%)	I&C (%)	I&D (%)	O&Q (%)	O&I (%)
M1	20.2	18.7	2.1	22.4	25.8	0.5	--	--	1.6	1.8	2.7	0.4
M2	17.5	14.1	1.8	36.2	21.5	0.3	0.6	--	1.7	0.8	2.0	1.2
M3	20.4	29.0	1.3	26.3	14.6	0.2	0.2	0.5	1.2	0.7	0.3	0.3
M4	18.7	21.1	1.5	33.4	17.4	0.2	1.3	0.4	1.1	0.5	0.9	0.3
M5	25.8	26.1	2.1	14.6	20.5	0.06	1.4	0.6	2.1	1.5	0.6	--
M6	23.5	24.5	1.8	19.4	22.6	0.3	0.8	--	1.2	0.7	0.2	0.5
M7	19.4	22.4	2.3	23.9	23.1	0.1	--	0.6	0.5	1.0	1.5	0.8
Mean	20.7±2.7	22.3±4.6	1.8±0.3	25.1±7.0	20.7±3.4	0.2±0.1	0.9±0.4	0.5±0.08	1.3±0.5	1.0±0.4	1.2±0.9	0.6±0.3

292 Note: Results were obtained from seven specimens of carbonate-rich Longmaxi shale. The labels 'C', 'D', 'Q', 'I', and 'O' represent calcite, dolomite,
 293 quartz, illite, and organic, respectively. The C&Q and D&Q phases are classified as brittle mixtures, whereas the I&O phase is classified as a ductile
 294 mixture. The I&C, I&D, and I&Q phases are classified as composite mixtures.

295

296 The digital mineralogy maps also illustrate the complex microstructure of the
297 Longmaxi shale, with a wide range of particle sizes for each mineral phase. **Fig. 8** shows a
298 representative result of the studied shale's cumulative particle area distribution functions
299 (measured on specimen M5). This data reveals that the carbonate minerals (calcite and
300 dolomite) were associated with larger particles than quartz, illite, and pyrite. Given that the
301 maximum penetration depth for the grid indentation tests ranged from 100 to 400 nm;
302 hence, the projected area of an indentation interaction volume ranged from 5 to 15 μm^2 .
303 Therefore, **Fig. 8** shows that the indentation footprint can exceed up to 20% of the quartz,
304 illite, and pyrite particles but only 5% for calcite and dolomite. The high proportion of fine
305 particles ($\leq 15 \mu\text{m}^2$) increases the probability that a mixture of mineral phases will affect
306 the indentation measurements and corresponding engineering properties. More detailed
307 observations from the SEM/BSE images showed two distinct morphologies of quartz, illite,
308 and pyrite minerals within the Longmaxi shale: 1) larger intact particles and 2) porous
309 aggregates of fine grains with nano-scale interparticle pores. It should be noted that
310 particles or pores with a size smaller than the pixel size of the digital mineralogy map (300
311 nm \times 300 nm) cannot be detected in this analysis. Thus, as a result, the curve of particle
312 area distribution for illite includes both the illite particles and the nano-porous aggregates
313 of illite.
314

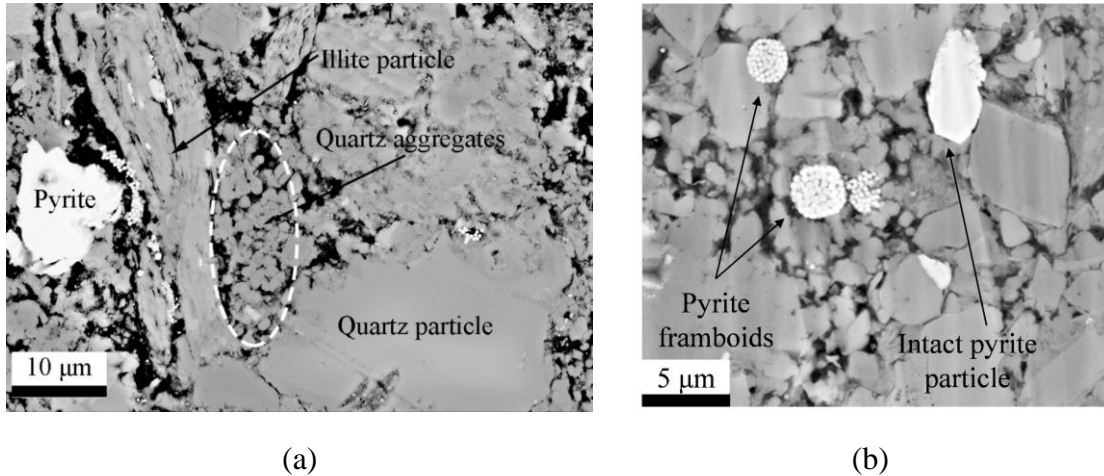


315

316 **Fig. 8.** Cumulative particle area distribution functions of calcite, dolomite, quartz, and pyrite phases
 317 measured in sample M5. The projected area of an indentation interaction volume can be up to $15 \mu\text{m}^2$,
 318 corresponding to $\sim 20\%$ for quartz, pyrite, and illite phases but only $\sim 5\%$ for calcite and dolomite.

319 **Fig. 9a** illustrates the co-existence of these morphologies for quartz, for which there
 320 was a significant contrast in individual particle size. These observations were consistent
 321 with results reported by Dong et al. (2019) and Xu et al. (2021), who also identified
 322 different forms of quartz in the Longmaxi shale. Similarly, the Longmaxi shale specimens
 323 included isolated larger pyrite particles and framboidal structures (**Fig. 9b**) that have been
 324 reported for other shales (e.g., Opalinus (Seiphoori et al. 2017)). In contrast, carbonate
 325 minerals were mostly found as isolated particles.

326



327 **Fig. 9.** Representative BSE image showing granular aggregates and isolated particles of mineral phases
 328 in shale: (a) quartz and (b) pyrite.

329

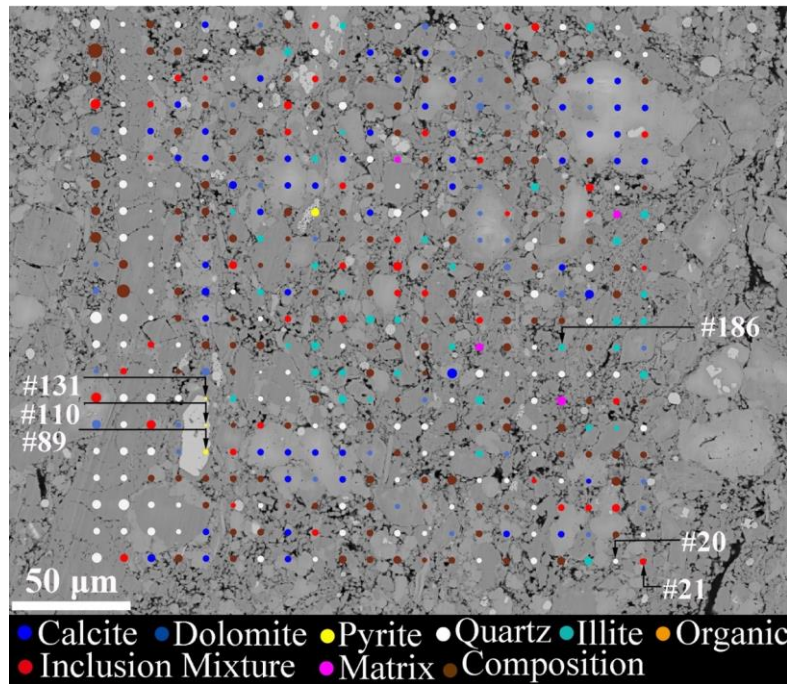
330 **3.2 Mechanical Properties of Mineral Phases from Grid Nanoindentation**

331 **Fig. 10** shows the local mineral phases at the locus of each indentation superimposed
 332 with the BSE image. Here, nine distinct mineral phases are identified, including six pure
 333 minerals (cf. Table 1 including organics), and three mixtures (i.e., brittle, ductile, and
 334 composite). Notably, although mixed phases characterize only 5.5% of the ROI surface
 335 area at the pixel scale (**Fig. 7**), 30 - 40% of the indentation footprints were classified as
 336 mixtures. This is due to the greater size of the indentation interaction volume (up to $1\mu\text{m} \times$
 337 $1\mu\text{m}$) when compared to the pixel size ($300\text{ nm} \times 300\text{ nm}$), which in turn resulted in a
 338 higher probability of measuring a mixture. **Figs 11a** and **11b** illustrate in more detail the
 339 accuracy of the indentation-mineral map by interpreting the indentation footprints and
 340 mineralogy of the randomly selected indent locations (as shown in **Fig. 10**). These
 341 examples show that the proposed coupled analysis of grid-nanoindentation and in-situ
 342 mineralogical identification provides a precise and reliable toolkit for identifying nano-
 343 scale mechanical mineralogical information in a complex composite material such as shale.

344 All the indentation data from grid indentation experiments on specimens M3 - M7 (in
 345 total $441 \times 5 = 2205$ indentations) were integrated. These data provided sufficient

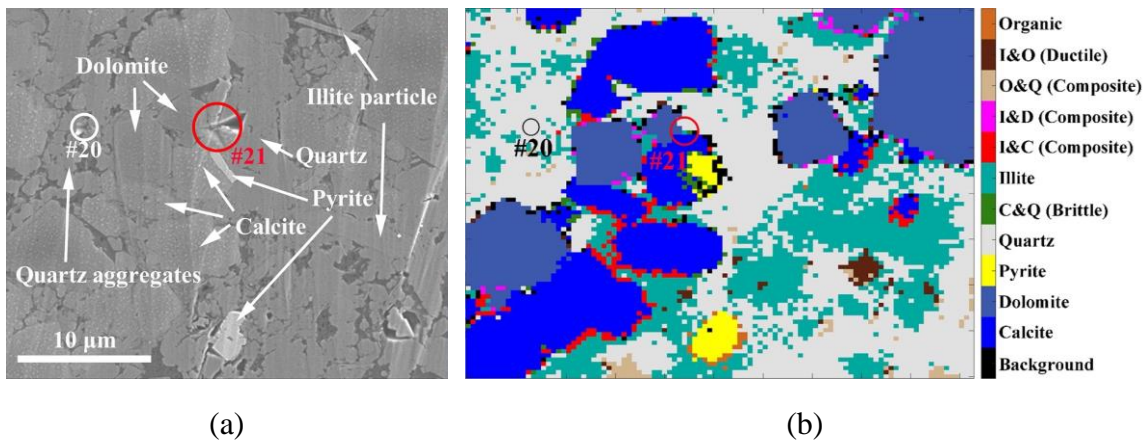
346 information for statistical analyses of each phase's mechanical properties and area
 347 fractions. Area fractions of the five pure mineral phases obtained from the statistical
 348 analysis were consistent with those measured from the in-situ mineralogical identification
 349 (Table 1).

350



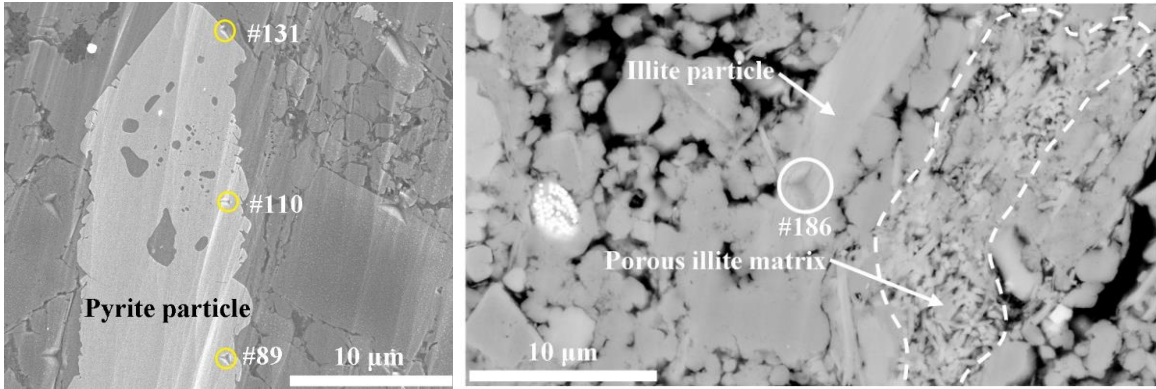
351

352 **Fig. 10.** Indentation-mineral map (sample M2) showing local mineral phases at the locus of each
 353 indentation superimposed with the BSE image. Indentation points are randomly selected to verify the
 354 accuracy of the measured indentation-mineral map.



(a)

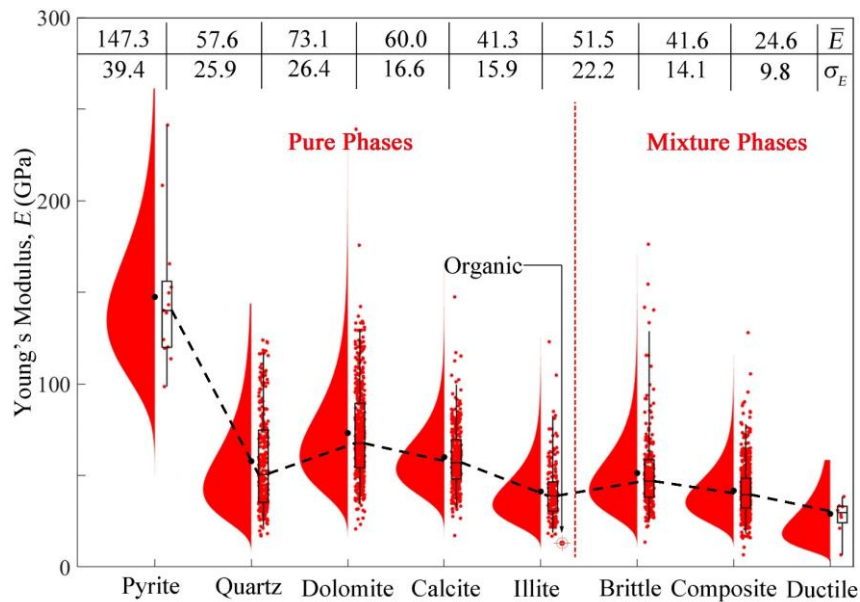
(b)



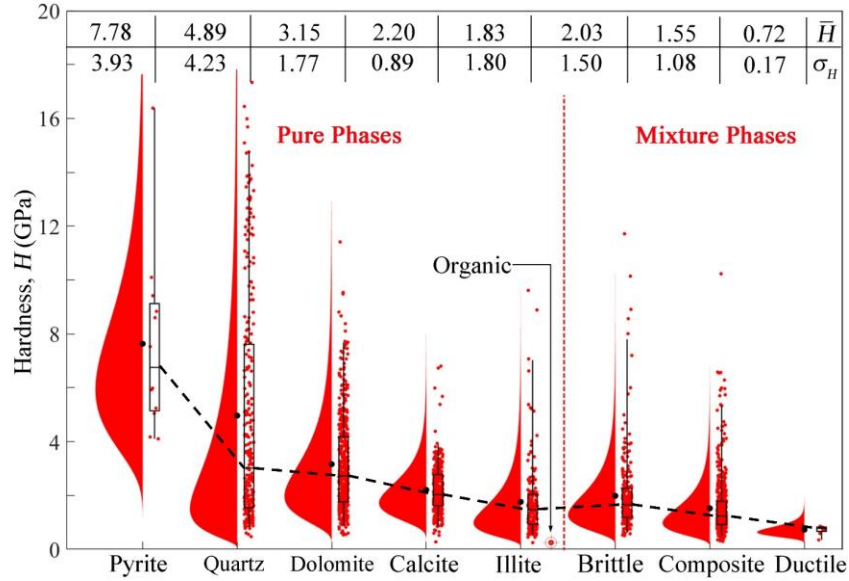
(c)

(d)

355 **Fig. 11.** Verification of the indentation-mineral map: a) Indentation footprints on a quartz phase (indent
 356 #20) and the brittle mineral mixtures (indent #21). b) Local mineralogy of indents #20 and #21. c)
 357 Indentation footprints on a single pyrite particle (indents #89, #110, #131), and d) indentation footprint
 358 on an illite particle (indent #186). These observations result from high-magnification SEM imaging and
 359 BSE imaging, respectively. The residual footprints of the selected points are circled in the SEM and
 360 BSE images.



(a)



(b)

361 **Fig. 12.** Mechanical properties of the mineral phases from grid nanoindentation of M1-M7 specimens:
 362 a) Young's modulus and b) hardness. The data are presented using a raincloud format that combines
 363 conventional boxplots with median, interquartile range (IQR) box, and outlier whiskers (upper quartile
 364 + 1.5×IQR and lower quartile - 1.5×IQR); together with interpretations assuming a single lognormal
 365 distribution function for each phase (expectation and standard deviation properties are reported in the
 366 inset in each figure). The black dots at the bottom of each distribution show the positions of the
 367 expectation (\bar{E} and \bar{H}).

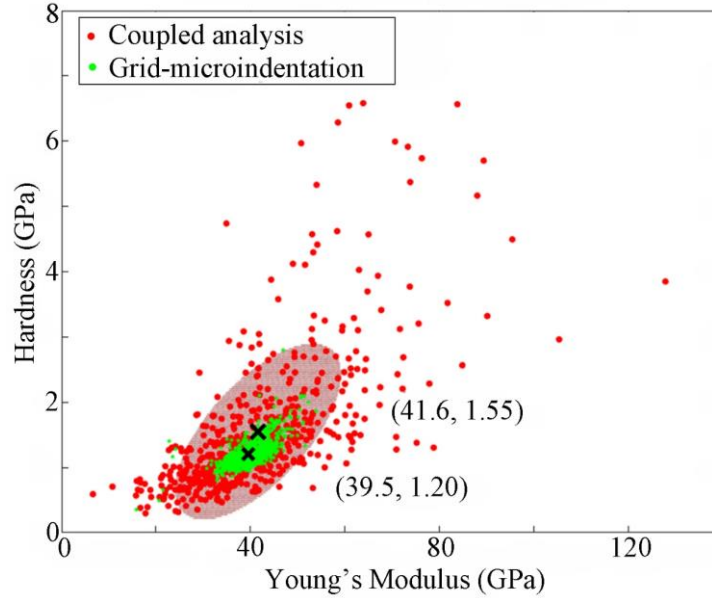
368

369 **Figs. 12a, 12b** show raincloud plots (Allen et al. 2019) of Young's modulus, E , and
 370 hardness, H , computed from grid nanoindentation on the Longmaxi shale for five pure
 371 mineral phases and three mixed phases. These figures combine boxplots of individual
 372 indents with an interpretation assuming that these properties can be described by a single
 373 lognormal distribution for each classified phase. The data was relatively sparse for the
 374 organic phase, and the properties of the organics were reported using a mean value ($E =$
 375 8.2GPa and $H = 0.95$ GPa), which is consistent with results reported in the literature by
 376 Eliyahu et al. (2015), Li et al. (2018), and Shukla et al. (2013). In addition, the boxplot data

377 for quartz and illite show significant skewness (particularly for H , **Fig. 12b**), which
378 indicates that the structures of the mechanical data of quartz and pyrite phases are not
379 monophasic. The skewness confirms prior observations that particle morphology (i.e.,
380 large intact particles vs. nano-porous aggregates of quartz and illite particles) affects the
381 results. The statistical mean of Young's modulus of clay phase shown in **Fig. 12b** (i.e.,
382 41.3 GPa) is greater than the results from some other prior studies (Bobko and Ulm 2008;
383 Liu et al. 2018). This is because the indentation data of the clay phase obtained from the
384 coupling analysis incorporate the measurement of both the intact clay particles and the
385 nano-porous clay aggregates. However, in prior studies, the indentation measurement
386 mainly focused on the porous clay composite, which has a much lower modulus and
387 hardness than those of the intact illite particles. A comparison between Young's modulus
388 and hardness of the five main mineral phases measured in this study and those reported in
389 prior publications are summarized in **Table 2**.

390 The data of the composite mixture phase obtained from the above coupled analysis can
391 be compared to measurements performed at a mesoscopic scale, beyond which the
392 mechanical response is homogeneous. **Fig. 13** compares Young's modulus and hardness
393 values of the composite mixture phase with microindentation data (penetration depths 8 -
394 10 μm) reported for the very same specimens of Longmaxi shale (Du et al. 2021). While
395 there is a much larger scatter in properties nanoindentation determined at the nanoscale
396 (reflecting the different phase mixtures), the two data sets show very similar mean values
397 of the two-dimensional Gaussian distribution. This result indicates that the homogenized
398 mechanical properties of complex composite materials such as shale can be assessed by its
399 nano/microscale representative unit composed of both the brittle and ductile mineral
400 phases.

401



402

403 **Fig. 13.** Comparison between the mechanical properties (E and H) of the composite phase extracted
 404 from the coupled analysis of nanoindentation ($h = 100 - 400$ nm; red dots) and the homogenous
 405 mechanical properties measured by grid microindentation with characteristic indentation depth $h = 8-$
 406 10 μm (green dots) (Du et al. 2021). Values in the brackets show the statistical mean of Young's modulus
 407 and hardness. The shaded ellipsoid is drawn based on the statistical confidence level of 95% and the
 408 covariance matrix, which determines the length of the major and minor axes, and the orientation of the
 409 axes, respectively.

410

411 3.3 Effects of Particle Size on Mechanical Properties

412 Determining the 'characteristic' lengths of the constituent mineral phases is essential
 413 for extracting their mechanical properties from the grid nanoindentation technique. By
 414 assuming the particles for each phase are spherical with a diameter, D , and that the
 415 indentation interaction volume is five times greater than the indentation depth h , Ulm and
 416 Abousleiman (2006) proposed that a ratio $h/D < 1/10$, will allow a reliable interpretation
 417 of mechanical properties for the constituent phases. However, this assumption does not
 418 consider indentation footprints closer to the edge of a particle, where a mixture of phases
 419 influences the mechanical response. Furthermore, the probability of indenting at the center

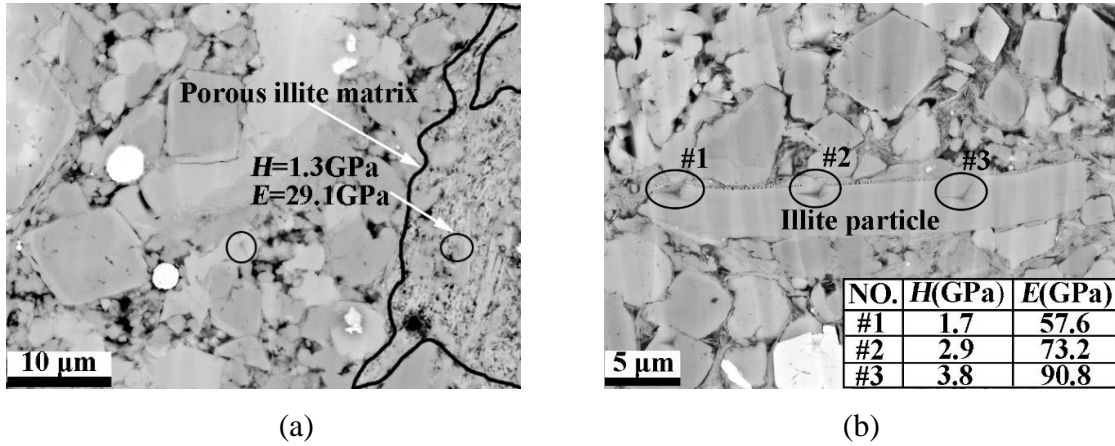
420 of a spherical particle is negligible, and hence, the characteristic length is generally
421 underestimated.

422 In this study, the critical characteristic lengths of the constituent mineral phases are
423 determined based on a probabilistic analysis. Considering a nanoindentation grid randomly
424 performed on a ROI, the mechanical properties of a given constituent mineral phase require
425 an adequate surface area for the indentation footprint within a single particle. The footprint
426 should be located at a minimum distance of $3h$ from the particle boundary to avoid the
427 influence of adjacent phases or pores. As a result, compared to the maximum indentation
428 depth, the particle area should be large enough to ensure that the probability of the
429 indentation loci within the applicable area, η , obeys the conservative rule of thumb, i.e., η
430 = 90%. Such a rule makes it possible to extract the mechanical properties of a specific
431 constituent phase by statistical analysis of all the particles of that phase. Therefore, the
432 critical characteristic length for measuring the mechanical properties of the constituent
433 phases can be determined as follows:

$$434 \quad \pi(R_c - 3h)^2 / \pi R_c^2 = 0.9 \quad (6)$$

435 where R_c is the particle radius. In this study, maximum indentation depths range from 100
436 to 200 nm for the pure mineral phases (i.e., calcite, dolomite, quartz, pyrite, and illite).
437 Therefore, the characteristic length and area of the pure mineral phases are about 5.8 - 11.7
438 μm and 100 - 430 μm^2 , respectively, i.e., up to 10 times greater than that proposed in prior
439 research.

440 The skewed distributions of mechanical properties for quartz and illite phases in **Fig.**
441 **12** suggest that the pure mineral phases must be partitioned to reflect two or more particle
442 structures. We have investigated particle size effects for quartz and illite phases based on
443 detailed observations of their particle morphology. For example, **Figs. 14a** and **14b**
444 compare nanoindentation values of E and H for nano-porous illite aggregate with those of
445 a much larger intact particle. The intact illite phase has a much higher modulus and
446 hardness than those of the nano-porous phase.



448 **Fig. 14.** BSE images of illite phase in Longmaxi shale samples. a) Nano-porous illite matrix with much
 449 lower hardness and Young's modulus than b) Intact illite particle. The residual indentation footprints
 450 are circled in the images.

451

452 The Bayesian Information Criterion (BIC) and Multidimensional Gaussian Mixture
 453 Model (GMM) (Abedi et al. 2016; Deirieh et al. 2012) were used to identify and classify
 454 morphological components for illite and quartz:

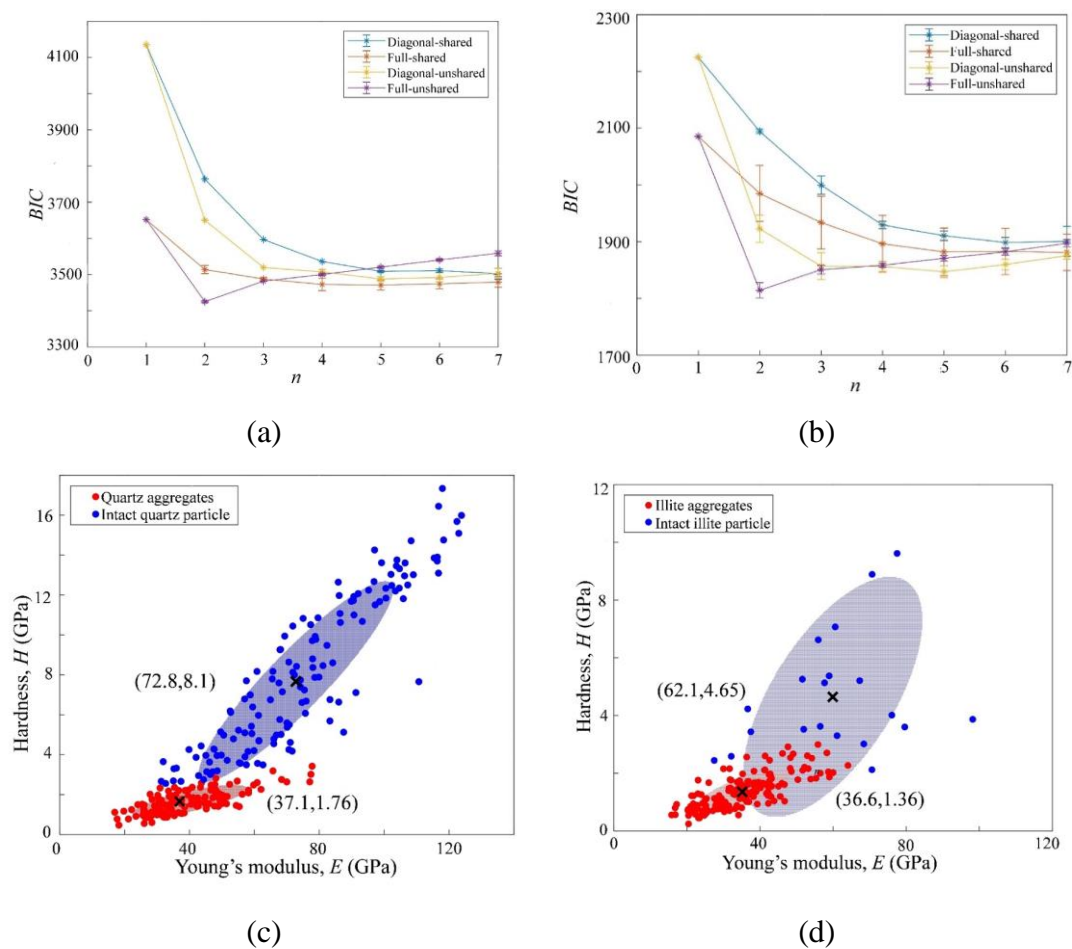
$$455 \quad BIC = -2\log\hat{L}(\theta) + n\log(N) \quad (7)$$

$$456 \quad j=1, n; D(X_i; \mu_j^X, s_j^X) = \frac{1}{s_j^X \sqrt{2\pi}} \int_{-\infty}^{X_i} \exp\left(-\frac{(u-\mu_j^X)^2}{2(s_j^X)^2}\right) du \quad (8)$$

457 where $\log\hat{L}(\theta)$ denotes the value of the maximized loglikelihood objective function, n is
 458 the number of components, and N is the number of data points, X_i is the i^{th} mechanical
 459 data, μ is the statistic mean, and s is the covariance matrix, which is a square matrix giving
 460 the covariance between each pair of elements of a given vector.

461 BIC analyses are performed 500 times for each preset component number n (from 2 to
 462 10) and each type of covariance matrix (diagonal or full; shared or unshared) to avoid a
 463 random error. The covariance matrix determines the shape of the confidence ellipsoid
 464 drawn over each cluster. In this study, we investigated whether the covariance matrices are
 465 diagonal or full, and whether all components have the same covariance matrix (shared or
 466 unshared). **Figs. 15a** and **15b** summarize the BIC analysis for quartz and illite phases,

467 respectively, indicating that a two-component mixture ($n = 2$) with a full-unshared
 468 covariance matrix provides the best representation. The modulus and hardness of these
 469 intact particles and nano-porous aggregates are then extracted by GMM clustering, as
 470 shown in **Figs. 15c** and **15d**. The shaded ellipsoids are generated based on the statistical
 471 confidence level of 95% and the covariance matrix, which determines the length of the
 472 major and minor axes, and the orientation of the axes, respectively.
 473



474 **Fig. 15.** Refined mechanical properties obtained by BIC and GMM analysis for quartz and illite. a) and
 475 b) Optimal components ($n=2$) based on BIC analysis for quartz and illite, respectively; c) and d) GMM
 476 analyses used to establish statistical mean values of Young's modulus and hardness for the intact and
 477 nano-porous aggregate components of quartz and illite, respectively.

478

479 To further address the effect of particle size on the mechanical properties, the
480 measured Young's modulus and hardness of a pure mineral phase were linked to the
481 particle sizes obtained from the edge detection algorithm. In all five pure mineral phases
482 in the Longmaxi shale (i.e., excluding organics), Young's modulus and hardness initially
483 increased with the particle area and then were relatively constant after the particle area
484 exceeded a specific threshold value. Young's modulus and hardness of intact mineral
485 particles were thus obtained (**Table 2**). Compared to the results from the coupled analysis
486 only (**Fig. 12**), with these considerations of particle size effects, the mechanical properties
487 of the constituent phases were further refined and show a better agreement with the values
488 for the same mineral phases reported in the literature, as shown in **Table 2**.

489 **Table 2**

490 Summary of Young's modulus and hardness of the 5 main mineral phases in Longmaxi shale samples obtained in this study and prior publications

Mineral Phase	Coupled analysis (Fig. 12)		Refinement by BIC & GMM (Fig. 15)		Results for Intact Particles (> threshold size)		<i>Published Results</i>		
	<i>E</i> (GPa)	<i>H</i> (GPa)	<i>E</i> (GPa)	<i>H</i> (GPa)	<i>E</i> (GPa)	<i>H</i> (GPa)	<i>E</i> (GPa)	<i>H</i> (GPa)	<i>Source</i>
Calcite	60.0	2.20	64.3	2.4	61.2	2.3	73-83	2.1-2.4	(1)
Dolomite	57.6	3.15	85.9	4.9	93.1	4.7	53-82	3.5-7.5	(2)
Quartz	73.1	4.89	72.8	8.10	69.3	6.9	82-96	13.3-14.8	(1)
Pyrite	147.3	7.78	--	--	226.6	13.6	264-330	16-27	(3)-(6)
Illite	41.3	1.83	62.1	4.65	71.1	3.9	62	--	(7)

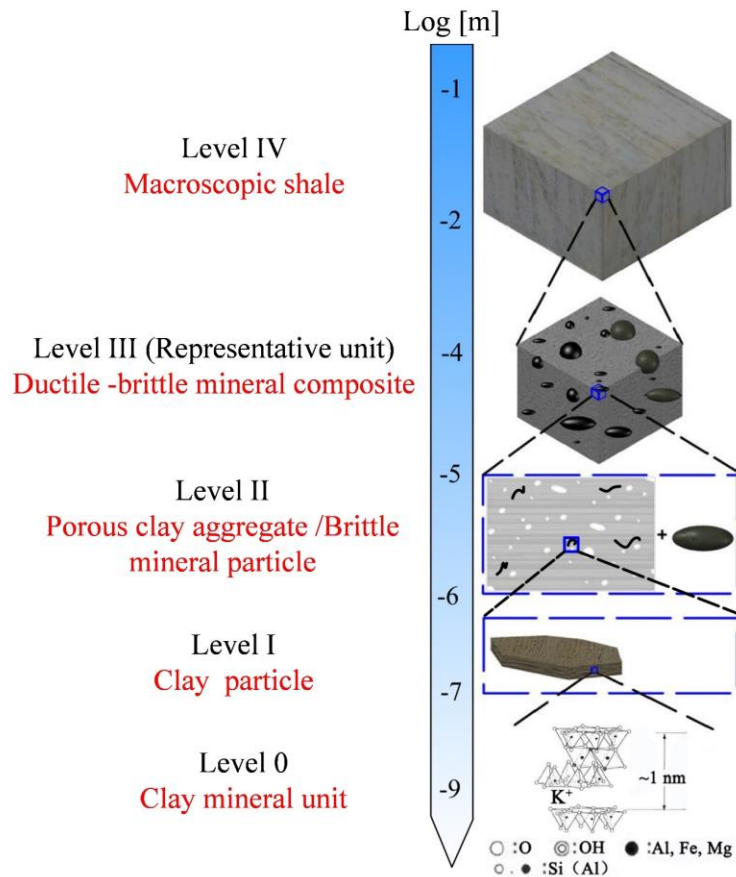
491 Note: (1) Broz et al. (2006); (2) Viktorov et al. (2014); (3) Li et al. (2022); (4) Kumar et al. (2012); (5) Aguilar-Santillan (2008); (6) Loberg et al.

492 (1985); (7) Xian et al. (2019)

493

494 **4 Discussion**

495 Shales are composite materials with high heterogeneity and complex multi-phase
496 characteristics. **Fig. 16** presents a conceptual 5-level (multi-scale) representation of shale
497 extending from the nanoscale clay unit to the centimeter-scale macroscopic shale.
498



499

500

Fig. 16. Multi-scale model of shale structure.

501

502 Level 0 corresponds to the elementary unit of clay minerals at the nanometer scale
503 (0.7 nm and 1.0 nm in thickness for the 1:1 and 2:1 phyllosilicate clay minerals,
504 respectively (Zhang et al. 2010)). Level I corresponds to the aggregated clay, which
505 typically comprises assemblies of particles in face-face configurations: illite aggregates

506 generally are up to 10 nm thick with surface dimensions ~500 - 1500 nm (Nadeau 1985).
 507 Level II is the scale of the ductile porous clay/organic aggregate and the brittle mineral
 508 particles. Level III corresponds to the representative unit of the macroscopic shale at the
 509 submillimeter scale, including both the ductile and brittle minerals. Thus, this scale is
 510 considered the elementary building block of shale. Level IV is the scale of macroscopic
 511 shale, which is the object of conventional, macroscopically-homogeneous laboratory
 512 studies. Precise prediction and characterization of the multi-scale mechanical properties of
 513 shale are of great scientific importance and engineering significance.

514 Upscaling of Level II to III has been widely carried out in prior studies using self-
 515 consistent and Mori-Tanaka approaches (Liu et al. 2018; Liu et al. 2022; Luo et al. 2021).
 516 In this study, a multi-scale model for upscaling mineral particles (Level I) to their nano-
 517 porous aggregates (Level II) was analyzed for the first time based on a self-consistent
 518 scheme for granular morphology, accounting for the nanoscale porosity of shale materials
 519 (Seiphoori et al. 2017). Young's moduli of Longmaxi shale samples at Levels I and II are
 520 obtained by the coupled analysis described in this study. These experimental data can
 521 provide both the input parameters and the experimental validation for the multi-scale
 522 mechanical model.

523 In the case of linear, isotropic, and elastic behavior of the mineral phases, a self-
 524 consistent model (Dormieux et al. 2006; Zaoui 2002) was established for homogenizing
 525 the stiffness of a mixture with granular morphology:

$$526 \quad K_{\text{hom}} = \sum_i \varphi_i K_i (1 + \alpha_0 (\frac{K_i}{K_{\text{hom}}} - 1))^{-1} \left[\sum_i \varphi_i (1 + \alpha_0 (\frac{K_i}{K_{\text{hom}}} - 1))^{-1} \right]^{-1} \quad (9)$$

$$527 \quad G_{\text{hom}} = \sum_i \varphi_i G_i (1 + \beta_0 (\frac{G_i}{G_{\text{hom}}} - 1))^{-1} \left[\sum_i \varphi_i (1 + \beta_0 (\frac{G_i}{G_{\text{hom}}} - 1))^{-1} \right]^{-1} \quad (10)$$

528 where K_{hom} and G_{hom} are the homogenized bulk modulus and shear modulus,
 529 respectively; K_i , G_i and φ_i are the bulk modulus, shear modulus, and volume fraction of

530 the i -th phase, respectively. Finally, α_0 and β_0 are defined by $\alpha_0 = \frac{3K_{\text{hom}}}{3K_{\text{hom}} + 4G_{\text{hom}}}$, and

531
$$\beta_0 = \frac{6(K_{\text{hom}} + 2G_{\text{hom}})}{5(3K_{\text{hom}} + 4G_{\text{hom}})}.$$

532 The upscaling of strength properties requires the use of non-linear homogenization
533 theory (Bobko et al. 2011):

534
$$H_{\text{hom}} = h_s \times \Pi_H(\eta, \mu) \quad (11)$$

535 where Π_H is a dimensionless function to be developed, H_{hom} and h_s are the
536 homogenized hardness and the particle hardness, respectively, and η and μ are the solid
537 packing density and friction coefficient, respectively. Based on data analysis, Gathier
538 (2008) obtained the scaling relations between the particle hardness, h_s , and the
539 homogenized hardness, H_{hom} , for a porous composite exhibiting self-consistent
540 morphology (after Bobko et al. (2011)):

541
$$\Pi_H(\eta, \mu) = \Pi_1(\eta) + \mu(1-\eta)\Pi_2(\eta, \mu) \quad (12)$$

542
$$\Pi_1(\eta) = \frac{\sqrt{2(2\eta-1)-(2\eta-1)}}{\sqrt{2}-1} [1-5.3678(1-\eta)+12.1933(1-\eta)^2-10.3071(1-\eta)^3] \quad (13)$$

543
$$\Pi_2(\eta, \mu) = \frac{2\eta-1}{2} [6.7374-39.5893(1-\eta)+34.3216(1-\eta)\mu-21.2053\mu^3] \quad (14)$$

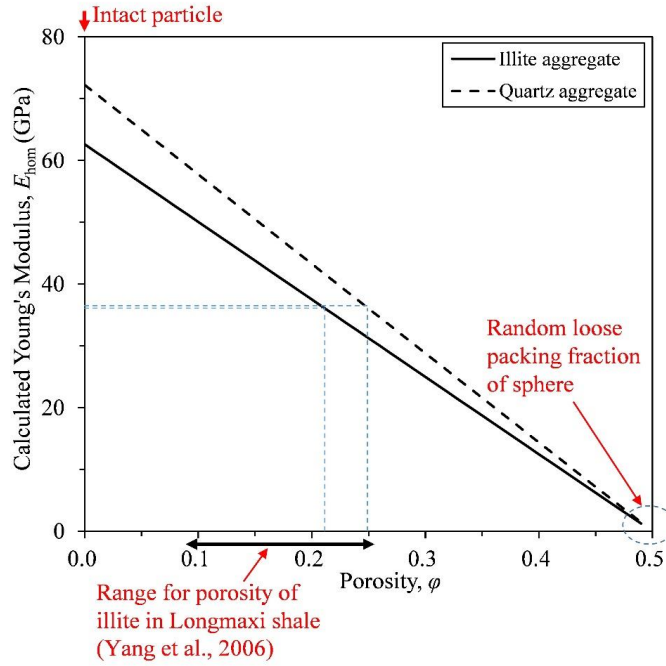
544 The quartz and illite phases of Longmaxi shale include intact particles and nano-
545 porous aggregates (level II; **Fig. 15**) that can be considered as a granular material and
546 upscaled using self-consistent assumptions. Young's modulus and hardness of the intact
547 particles are determined by the GMM fitting of the grid nanoindentation data. However,
548 the packing density/porosity of the nano-porous aggregates ($\eta = 1-\phi$) is not measured
549 directly in this study.

550 **Fig. 17a** shows the relationships of the homogenized stiffness [Eqs. (9), and (10)] as
551 a function of the stiffness of intact particles (i.e., at $\phi = 0$) and the porosity of the nano-
552 aggregates for illite and quartz phases. These results show that the self-consistent
553 formulation explains the difference in mean values of E for intact and nano-porous
554 aggregates with $\phi = 0.21, 0.25$ for illite and quartz, respectively. The estimate of nano-

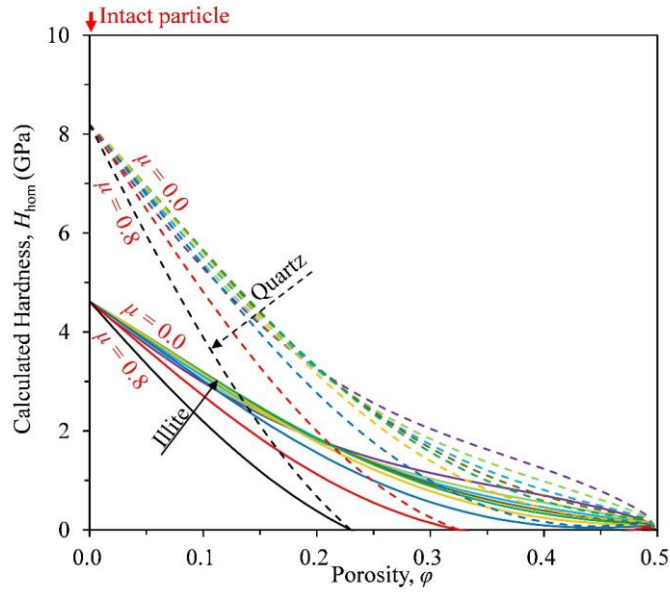
555 porosity for illite is also within the range reported from nitrogen adsorption measurements
556 on Longmaxi shale by Yang et al. (2016). The increased porosity results in lower
557 homogenized stiffness and hardness for both the illite and quartz aggregates. As the
558 porosity equals zero, the composite material becomes an intact particle. Thus, the
559 calculated stiffness and hardness [E, H] reflect the properties of the intact illite and quartz
560 particles, i.e., [62.1 GPa/4.65 GPa] and [72.8 GPa/8.10 GPa], respectively.

561 **Fig. 17b** shows the homogenized hardness for the nano-porous quartz and illite
562 aggregates [based on Eqs. (9) - (11)] as functions of intact particle hardness, nano-porosity,
563 and selected values of the friction coefficient μ . There have been extensive studies of the
564 inter-particle friction for quartz (e.g., summarized in Terzaghi et al., 1996), suggesting an
565 average value $\mu = 0.4$, and thus an estimated homogenized hardness, $H = 2.4$ GPa. This
566 value is higher than the mean (1.8 GPa) reported in **Fig. 15a** but is within the range
567 measured for nano-porous quartz in Longmaxi shale. Similarly, the interparticle friction of
568 illite has been reported in the range $\mu = 0.40 \pm 0.04$, corresponding to a homogenized
569 hardness, $H = (1.7 \pm 0.02)$ GPa from the self-consistent analyses (**Fig. 17b**), which is within
570 the range identified by GMM analyses of nano-porous illite (**Fig. 15b**).

571



(a)



(b)

572

573

574

575

576 **Fig. 17.** Self-consistent homogenized a) Young's modulus, E ; and b) hardness, H , for nano-porous
 577 quartz and illite aggregates as functions of assumed nano-porosity, ϕ . H values are shown at selected
 578 friction ratios, $\mu = 0.0 - 0.8$ (0.1 interval).

579

580 **5 Conclusions**

581 In this study, we developed a coupled analysis of grid nanoindentation and in-situ
582 mineralogical identification considering the particle size effect to access the mechanical
583 properties of the constituent mineral phases. Furthermore, multi-scale mechanical models
584 for upscaling the elastic stiffness and strength properties were established, considering the
585 self-consistent scheme for granular morphology to link the microscopic characteristics with
586 the multi-scale mechanical properties of shales. The key conclusions of this study are as
587 follows:

- 588 1. By combining digital images of mineral distribution and control coordinates for
589 grid nanoindentation, Mechanical properties (hardness and Young's modulus) for
590 five pure mineral phases (i.e., calcite, dolomite, quartz, pyrite, and illite) and three
591 mineral mixture phases (i.e., brittle, ductile, and composite mixtures) are extracted
592 for specimens of carbonate-rich Longmaxi shale.
- 593 2. Threshold particle sizes were identified for estimating intact mineral properties
594 based on a probabilistic interpretation of the indentation footprint. The identified
595 characteristic length for extracting the mechanical properties of constituent
596 mineral phases from the grid nanoindentation technique is about 5.8 - 11.7 μm ,
597 i.e., up to 10 times greater than that proposed in prior research.
- 598 3. The mechanical properties of shale mineral phases are influenced by particle size
599 and morphology, particularly for quartz and illite phases. These phases are further
600 partitioned (through statistical BIC and two-dimensional GMM analyses) to
601 distinguish between the mechanical properties of individual particles and nano-
602 porous aggregates.
- 603 4. A multi-scale model for upscaling from mineral particles (Level I) to their nano-
604 porous aggregates (Level II) is analyzed for the first time based on a self-
605 consistent scheme for granular morphology. The self-consistent modeling

606 approach can explain the measured differences in elastic stiffness and hardness
607 properties of the mineral aggregates and their intact particles. This provides a clear
608 basis for upscaling properties from the microscopic characteristics (i.e., the
609 volume fractions and the mechanical properties of the intact mineral particles)
610 measured by the proposed coupling analysis.

611

612 **CRedit authorship contribution statement**

613 **Jianting Du:** Formal analysis, Investigation, Methodology, Writing – original draft.

614 **Andrew J. Whittle:** Conceptualization, Methodology, Funding acquisition, Project
615 administration, Supervision, Writing – review & editing. **Liming Hu:** Conceptualization,

616 Funding acquisition, Project administration, Supervision, Writing – review & editing.

617 **Thibaut Divoux:** Investigation, Project administration, Writing – review & editing. **Jay**

618 **N. Meegoda:** Supervision, Writing – review & editing.

619

620 **Declaration of Competing Interest**

621 The authors declare that they have no known competing financial interests or personal
622 relationships that could have appeared to influence the work reported in this paper.

623

624 **Data Availability**

625 Data will be made available on request.

626

627 **Acknowledgments:**

628 This research was funded by the National Natural Science Foundation of China
629 (Project No. 51979144, 51661165015, and 51323014) and the Open Research Fund
630 Program of State Key Laboratory of Hydroscience and Engineering (Project Number:
631 sklhse-2023-D-04). The authors gratefully acknowledge the support of the Concrete

632 Sustainability Hub in the MIT Department of Civil and Environmental Engineering for
633 access to facilities and assistance in conducting this research.

634

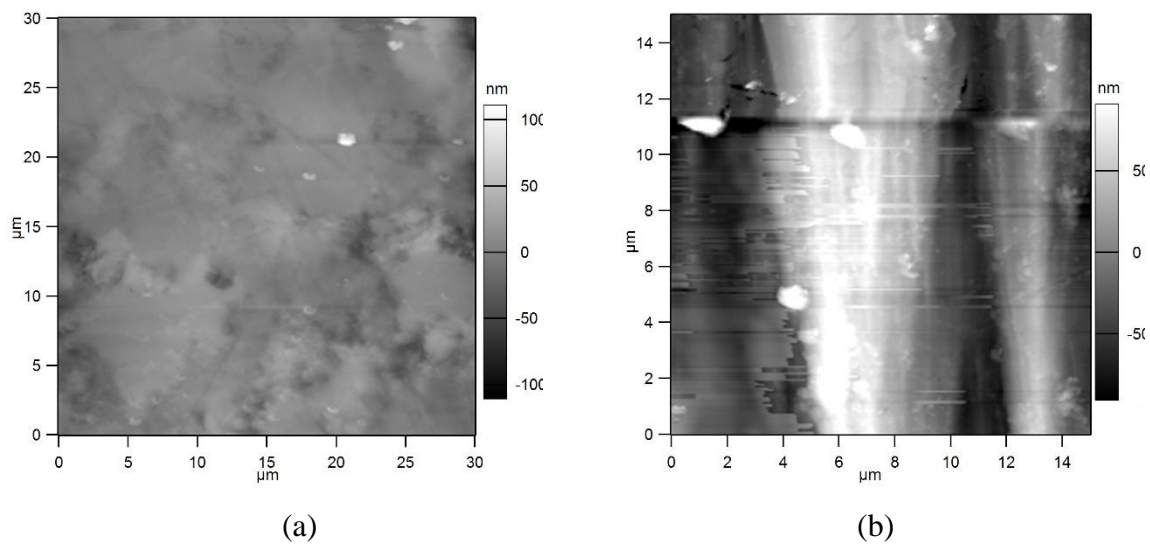
635 **Appendix A. Surface preparation**

636 *Argon Milling*

637 The trimmed shale samples are polished with the coarse abrasive paper into 1 cm × 1
638 cm × 0.5 cm thick blocks as required by the JEOL cross-section polisher. The maximum
639 accelerating voltage of 6 kV is applied to minimize the heat damage, and the milling
640 duration is set to 10 -12 h. Typically, 50 - 100 μm deep materials are removed from the
641 surface to ensure that the milled surface is free of mechanical polishing artifacts as well as
642 smearing due to razor blade cutting.

643 AFM roughness characterization of shale samples prepared by mechanical polishing
644 and Argon milling (**Fig. A1**) shows RMS roughness, $R_q = 15$ nm and 50 nm, respectively.
645 Trenching is a usually unwanted side effect of ion beam milling (Youngner and Haynes
646 1982), which may increase the roughness of a milled surface.

647

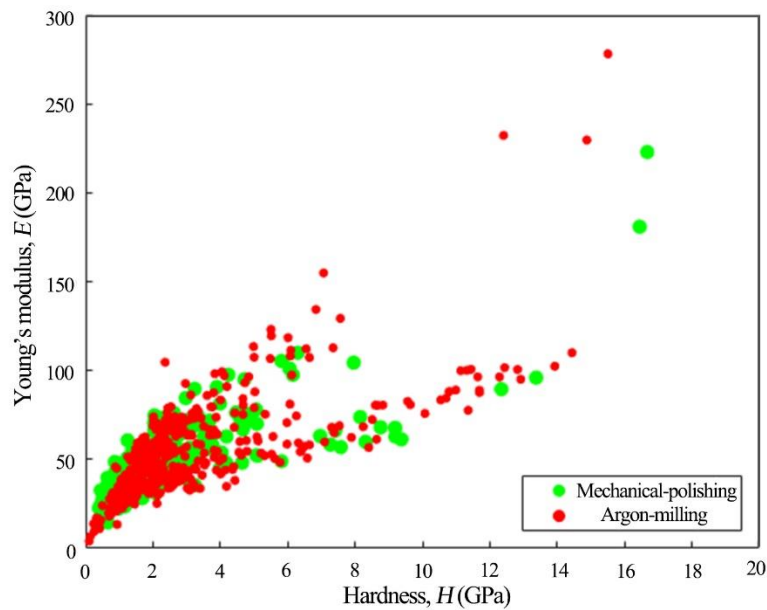


648 **Fig. A1. Representative AFM maps of interested regions prepared by mechanical polishing (a) and**
649 **Argon milling (b). The dimensions of AFM images are 30 μm by 30 μm and 15 μm by 15 μm,**
650 **respectively, and the measured surface roughness, $R_q = 16$ nm and $R_q = 50$ nm, respectively.**

651

652 The surface roughness effect on nanoindentation testing from mechanical polishing
653 and Argon milling is analyzed contrastively. As shown in **Fig. A2**, the Young modulus and
654 hardness data of the mechanical-polishing sample and Argon-milling sample are in good
655 accordance with each other, i.e., these two surface preparation create qualified surface
656 conditions for nanoindentation testing. Due to its ease of use and high efficiency,
657 mechanical polishing is employed for the surface preparation in this study.

658



659

660 **Fig. A2. Comparison of Young's modulus and hardness data between the mechanical-polishing**
661 **sample (green points) and Argon-milling sample (red points).**

662

663 **References**

664 Abedi, S., Slim, M., Hofmann, R., Bryndzia, T. & Ulm, F., 2016. Nanochemo-
665 mechanical signature of organic-rich shales: a coupled indentation-EDX analysis. *Acta*
666 *Geotech.* 11, 559-572. doi: <https://doi.org/10.1007/s11440-015-0426-4>.

667 Aguilar-Santillan, J., 2008. Elastic and hardness anisotropy and the indentation size
668 effect of pyrite (FeS₂) single crystal. *Acta Mater.* 56, 2476-2487. doi:
669 <https://doi.org/10.1016/j.actamat.2008.01.022>.

670 Allen, M., Poggiali, D., Whitaker, K.J., Marshall, T.R. & Kievit, R.A., 2019.
671 Raincloud plots: a multi-platform tool for robust data visualization. Wellcome Open
672 Research 4, 63. doi: <https://doi.org/10.12688%2Fwellcomeopenres.15191.1>.

673 Bobji, M.S. & Biswas, S.K., 1999. Deconvolution of hardness from data obtained
674 from nanoindentation of rough surfaces. J. Mater. Res. 14, 2259-2268. doi:
675 <https://doi.org/10.1557/JMR.1999.0302>.

676 Bobko, C.P., Gathier, B., Ortega, J.A., Ulm, F., Borges, L. & Abousleiman, Y.N.,
677 2011. The nanogranular origin of friction and cohesion in shale—A strength
678 homogenization approach to interpretation of nanoindentation results. Int. J. Numer. Anal.
679 Methods Geomech. 35, 1854-1876. doi: <https://doi.org/10.1002/nag.984>.

680 Bobko, C.P. & Ulm, F., 2008. The nano-mechanical morphology of shale. Mech.
681 Mater. 40, 318-337. doi: <https://doi.org/10.1016/j.mechmat.2007.09.006>.

682 Boosari, S.S.H., Aybar, U. & Eshkalak, M.O., 2015. Carbon Dioxide Storage and
683 Sequestration in Unconventional Shale Reservoirs. Journal of Geoscience and
684 Environment Protection 03, 7-15. doi: <http://dx.doi.org/10.4236/gep.2015.31002>.

685 Broz, M.E., Cook, R.F. & Whitney, D.L., 2006. Microhardness, toughness, and
686 modulus of Mohs scale minerals. Am. Mineral. 91, 135-142. doi:
687 <https://doi.org/10.2138/am.2006.1844>.

688 Chen, J., Lan, H., Macciotta, R., Wu, Y., Li, Q. & Zhao, X., 2018. Anisotropy rather
689 than transverse isotropy in Longmaxi shale and the potential role of tectonic stress. Eng.
690 Geol. 247, 38-47. doi: <https://doi.org/10.1016/j.enggeo.2018.10.018>.

691 Chen, P., Han, Q., Ma, T. & Lin, D., 2015. The mechanical properties of shale based
692 on micro-indentation test. Pet. Explor. Dev. 42, 723-732. doi:
693 [https://doi.org/10.1016/S1876-3804\(15\)30069-0](https://doi.org/10.1016/S1876-3804(15)30069-0).

694 Constantinides, G., Chandran, K.S.R., Ulm, F. & Van Vliet, K.J., 2006. Grid
695 indentation analysis of composite microstructure and mechanics: Principles and validation.
696 Materials Science and Engineering A-structural Materials Properties Microstructure and
697 Processing 430, 189-202. doi: <https://doi.org/10.1016/j.msea.2006.05.125>.

698 Dai, J., Zou, C., Liao, S., Dong, D., Ni, Y., Huang, J., Wu, W., Gong, D., Huang, S.
699 & Hu, G., 2014. Geochemistry of the extremely high thermal maturity Longmaxi shale gas,
700 southern Sichuan Basin. Org. Geochem. 74, 3-12. doi:
701 <https://doi.org/10.1016/j.orggeochem.2014.01.018>.

702 Deirieh, A., Ortega, J.A., Ulm, F. & Abousleiman, Y.N., 2012.
703 Nanochemomechanical assessment of shale: a coupled WDS-indentation analysis. Acta
704 Geotech. 7, 271-295. doi: <https://doi.org/10.1007/s11440-012-0185-4>.

705 Dong, T., He, S., Chen, M., Hou, Y., Guo, X., Wei, C., Han, Y. & Yang, R., 2019.
706 Quartz types and origins in the paleozoic Wufeng-Longmaxi Formations, Eastern Sichuan
707 Basin, China: Implications for porosity preservation in shale reservoirs. Mar. Pet. Geol.
708 106, 62-73. doi: <https://doi.org/10.1016/j.marpetgeo.2019.05.002>.

709 Donnelly, E., Baker, S.P., Boskey, A.L. & Der Meulen, M.C.H.V., 2006. Effects of
710 surface roughness and maximum load on the mechanical properties of cancellous bone
711 measured by nanoindentation. *J. Biomed. Mater. Res. Part A* 77, 426-435. doi:
712 <https://doi.org/10.1002/jbm.a.30633>.

713 Dormieux, L., Kondo, D. & Ulm, F.-J. 2006. *Microporomechanics*. John Wiley &
714 Sons.

715 Du, J., Hu, L., Meegoda, J.N. & Zhang, G., 2018. Shale softening: observations,
716 phenomenological behavior, and mechanisms. *Appl. Clay Sci.* 161, 290-300. doi:
717 <https://doi.org/10.1016/j.clay.2018.04.033>.

718 Du, J., Whittle, A.J., Hu, L., Divoux, T. & Meegoda, J.N., 2021. Characterization of
719 meso-scale mechanical properties of Longmaxi shale using grid microindentation
720 experiments. *J. Rock Mech. Geotech. Eng.* 13, 555-567. doi:
721 <https://doi.org/10.1016/j.jrmge.2020.09.009>.

722 Durst, K., Backes, B. & Göken, M., 2005. Indentation size effect in metallic materials:
723 Correcting for the size of the plastic zone. *Scr. Mater.* 52, 1093-1097. doi:
724 <https://doi.org/10.1016/j.scriptamat.2005.02.009>.

725 Eliyahu, M., Emmanuel, S., Daystirrat, R.J. & Macaulay, C.I., 2015. Mechanical
726 properties of organic matter in shales mapped at the nanometer scale. *Mar. Pet. Geol.* 59,
727 294-304. doi: <https://doi.org/10.1016/j.marpetgeo.2014.09.007>.

728 Elliot, T.R. & Celia, M.A., 2012. Potential Restrictions for CO₂ Sequestration Sites
729 Due to Shale and Tight Gas Production. *Environ. Sci. Technol.* 46, 4223-4227. doi:
730 <https://doi.org/10.1021/es2040015>.

731 Gathier, B. 2008. *Multiscale strength homogenization: Application to shale*
732 *nanoindentation*, Massachusetts Institute of Technology.

733 Guo, Z., Li, X.-Y., Liu, C., Feng, X. & Shen, Y., 2013. A shale rock physics model
734 for analysis of brittleness index, mineralogy and porosity in the Barnett Shale. *J. Geophys.*
735 *Eng.* 10, 025006. doi: <https://doi.org/10.1088/1742-2132/10/2/025006>.

736 Jiu, B., Huang, W., He, M., Lv, C. & Liang, F., 2018. Quantitative analysis of micron-
737 scale and nano-scale pore throat characteristics of tight sandstone using matlab. *Applied*
738 *Sciences* 8, 1272. doi: <https://doi.org/10.3390/app8081272>.

739 Jiu, B., Huang, W. & Li, Y., 2020. An approach for quantitative analysis of
740 cementation in sandstone based on cathodoluminescence and MATLAB algorithms.
741 *Journal of Petroleum Science and Engineering* 186, 106724. doi:
742 <https://doi.org/10.1016/j.petrol.2019.106724>.

743 Kuila, U., McCarty, D.K., Derkowski, A., Fischer, T.B., Topór, T. & Prasad, M.,
744 2014. Nano-scale texture and porosity of organic matter and clay minerals in organic-rich
745 mudrocks. *Fuel* 135, 359-373. doi: <https://doi.org/10.1016/j.fuel.2014.06.036>.

746 Kumar, V., Sondergeld, C.H. & Rai, C.S. 2012. Nano to macro mechanical
747 characterization of shale. *SPE Annual Technical Conference and Exhibition*. Society of
748 Petroleum Engineers, San Antonio, Texas, USA.

749 Larsson, P., Giannakopoulos, A.E., Soderlund, E., Rowcliffe, D.J. & Vestergaard, R.,
750 1996. Analysis of Berkovich indentation. *Int. J. Solids Struct.* 33, 221-248. doi:
751 [https://doi.org/10.1016/0020-7683\(95\)00033-7](https://doi.org/10.1016/0020-7683(95)00033-7).

752 Li, C., Ostadhassan, M., Gentzis, T., Kong, L., Carvajalortiz, H. & Bubach, B., 2018.
753 Nanomechanical characterization of organic matter in the Bakken formation by
754 microscopy-based method. *Mar. Pet. Geol.* 96, 128-138. doi:
755 <https://doi.org/10.1016/j.marpetgeo.2018.05.019>.

756 Li, L., Huang, B., Tan, Y., Li, X. & Ranjith, P., 2022. Using micro-indentation to
757 determine the elastic modulus of shale laminae and its implication: Cross-scale correlation
758 of elastic modulus of mineral and rock. *Mar. Pet. Geol.* 143, 105740. doi:
759 <https://doi.org/10.1016/j.marpetgeo.2022.105740>.

760 Liu, K., Ostadhassan, M., Bubach, B., Ling, K., Tokhmechi, B. & Robert, D., 2018.
761 Statistical grid nanoindentation analysis to estimate macro-mechanical properties of the
762 Bakken Shale. *J. Nat. Gas Sci. Eng.* 53, 181-190. doi:
763 <https://doi.org/10.1016/j.jngse.2018.03.005>.

764 Liu, Y., Liu, A., Liu, S. & Kang, Y., 2022. Nano-scale mechanical properties of
765 constituent minerals in shales investigated by combined nanoindentation statistical
766 analyses and SEM-EDS-XRD techniques. *Int. J. Rock Mech. Min. Sci.* 159, 105187. doi:
767 <https://doi.org/10.1016/j.ijrmms.2022.105187>.

768 Liu, Y., Liu, S. & Kang, Y., 2021. Probing nanomechanical properties of a shale with
769 nanoindentation: heterogeneity and the effect of water–shale interactions. *Energy Fuels*
770 35, 11930-11946. doi: <https://doi.org/10.1021/acs.energyfuels.1c01328>.

771 Loberg, B.E., Háber, M. & Westberg, S.-B., 1985. Microhardness, reflectance and
772 unit cell length of pyrites from Swedish base metal ores. *Geologiska Föreningen i*
773 *Stockholm Förhandlingar* 107, 45-52. doi: <https://doi.org/10.1080/11035898509452612>.

774 Luo, S., Kim, D., Wu, Y., Li, Y., Wang, D., Song, J., DeGroot, D.J. & Zhang, G.,
775 2021. Big data nanoindentation and analytics reveal the multi-staged, progressively-
776 homogenized, depth-dependent upscaling of rocks' properties. *Rock Mech. Rock Eng.*
777 54, 1501-1532. doi: <https://doi.org/10.1007/s00603-020-02337-3>.

778 Luo, S., Lu, Y., Wu, Y., Song, J., DeGroot, D.J., Jin, Y. & Zhang, G., 2020. Cross-
779 scale characterization of the elasticity of shales: Statistical nanoindentation and data
780 analytics. *J. Mech. Phys. Solids* 140, 103945. doi:
781 <https://doi.org/10.1016/j.jmps.2020.103945>.

782 Mashhadian, M., Verde, A., Sharma, P. & Abedi, S., 2018. Assessing mechanical
783 properties of organic matter in shales: Results from coupled nanoindentation/SEM-EDX

784 and micromechanical modeling. *Journal of Petroleum Science and Engineering* 165, 313-
785 324.

786 Middleton, R.S., Viswanathan, H.S., Currier, R.P. & Gupta, R., 2014. CO₂ as a
787 fracturing fluid: Potential for commercial-scale shale gas production and CO₂
788 sequestration. *Energy Procedia* 63, 7780-7784. doi:
789 <https://doi.org/10.1016/j.egypro.2014.11.812>.

790 Nadeau, P., 1985. The physical dimensions of fundamental clay particles. *Clay Miner.*
791 20, 499-514. doi: <https://doi.org/10.1180/claymin.1985.020.4.06>.

792 Neuzil, C.E., 2013. Can Shale Safely Host U.S. Nuclear Waste. *Eos, Transactions*
793 *American Geophysical Union* 94, 261-262. doi: <https://doi.org/10.1002/2013EO300001>.

794 Oliver, W.C. & Pharr, G.M., 1992. An improved technique for determining hardness
795 and elastic modulus using load and displacement sensing indentation experiments. *J.*
796 *Mater. Res.* 7, 1564. doi: <https://doi.org/10.1557/JMR.1992.1564>.

797 Seiphoori, A., Whittle, A.J., Krakowiak, K.J. & Einstein, H.H., 2017. Insights into
798 diagenesis and pore structure of opalinus shale through comparative studies of natural and
799 reconstituted materials. *Clays Clay Miner.* 65, 135-153. doi:
800 <https://doi.org/10.1346/CCMN.2017.064055>.

801 Shukla, P., Kumar, V., Curtis, M., Sondergeld, C.H. & Rai, C.S. 2013.
802 Nanoindentation studies on shales. *47th US Rock Mechanics/Geomechanics Symposium*.
803 American Rock Mechanics Association, San Francisco, California, USA.

804 Simpson, G.J., Sedin, D.L. & Rowlen, K.L., 1999. Surface roughness by contact
805 versus tapping mode atomic force microscopy. *Langmuir* 15, 1429-1434. doi:
806 <http://dx.doi.org/10.1021/la981024a>.

807 Ulm, F. & Abousleiman, Y.N., 2006. The nanogranular nature of shale. *Acta Geotech.*
808 1, 77-88. doi: <https://doi.org/10.1007/s11440-006-0009-5>.

809 Ulm, F., Vandamme, M., Bobko, C.P., Ortega, J.A., Tai, K. & Ortiz, C., 2007.
810 Statistical Indentation Techniques for Hydrated Nanocomposites: Concrete, Bone, and
811 Shale. *J. Am. Ceram. Soc.* 90, 2677-2692. doi: <https://doi.org/10.1111/j.1551-2916.2007.02012.x>.

813 Veytskin, Y., Tammina, V.K., Bobko, C.P., Hartley, P.G., Clennell, M.B., Dewhurst,
814 D.N. & Dagastine, R.R., 2017. Micromechanical characterization of shales through
815 nanoindentation and energy dispersive x-ray spectrometry. *Geomech. Energy Environ.* 9,
816 21-35.

817 Viktorov, S., Golovin, Y.I., Kochanov, A., Tyurin, A., Shuklinov, A., Shuvarin, I. &
818 Pirozhkova, T., 2014. Micro-and nano-indentation approach to strength and deformation
819 characteristics of minerals. *J. Min. Sci.* 50, 652-659. doi:
820 <https://doi.org/10.1134/S1062739114040048>.

821 Wu, L.C. & Yu, C. 2012. Powder particle size measurement with digital image
822 processing using Matlab. *Advanced Materials Research*. Trans Tech Publ, 589-593.

823 Wu, Y., Li, Y., Luo, S., Lu, M., Zhou, N., Wang, D. & Zhang, G., 2020. Multiscale
824 elastic anisotropy of a shale characterized by cross-scale big data nanoindentation. *Int. J.*
825 *Rock Mech. Min. Sci.* 134, 104458. doi: <https://doi.org/10.1016/j.ijrmms.2020.104458>.

826 Xian, S., Jiang, S., Shuangfang, L., Zhiliang, H., Dongjie, L., Zhixuan, W. & Dianshi,
827 X., 2019. Investigation of mechanical properties of bedded shale by nanoindentation tests:
828 A case study on Lower Silurian Longmaxi Formation of Youyang area in southeast
829 Chongqing, China. *Pet. Explor. Dev.* 46, 163-172. doi: [https://doi.org/10.1016/S1876-](https://doi.org/10.1016/S1876-3804(19)30016-3)
830 [3804\(19\)30016-3](https://doi.org/10.1016/S1876-3804(19)30016-3).

831 Xu, H., Zhou, W., Hu, Q., Yi, T., Ke, J., Zhao, A., Lei, Z. & Yu, Y., 2021. Quartz
832 types, silica sources and their implications for porosity evolution and rock mechanics in
833 the Paleozoic Longmaxi Formation shale, Sichuan Basin. *Mar. Pet. Geol.* 128, 105036.
834 doi: <https://doi.org/10.1016/j.marpetgeo.2021.105036>.

835 Xu, J., Tang, X., Wang, Z., Feng, Y. & Bian, K., 2020. Investigating the softening of
836 weak interlayers during landslides using nanoindentation experiments and simulations.
837 *Eng. Geol.* 277, 105801. doi: <https://doi.org/10.1016/j.enggeo.2020.105801>.

838 Yang, R., He, S., Yi, J. & Hu, Q., 2016. Nano-scale pore structure and fractal
839 dimension of organic-rich Wufeng-Longmaxi shale from Jiaoshiba area, Sichuan Basin:
840 Investigations using FE-SEM, gas adsorption and helium pycnometry. *Mar. Pet. Geol.* 70,
841 27-45. doi: <https://doi.org/10.1016/j.marpetgeo.2015.11.019>.

842 Youngner, D. & Haynes, C., 1982. Modeling ion beam milling. *Journal of Vacuum*
843 *Science and Technology* 21, 677-680. doi: <https://doi.org/10.1116/1.571812>.

844 Zaoui, A., 2002. Continuum micromechanics: survey. *Journal of Engineering*
845 *Mechanics-ASCE* 128, 808-816. doi: [https://doi.org/10.1061/\(ASCE\)0733-](https://doi.org/10.1061/(ASCE)0733-9399(2002)128:8(808))
846 [9399\(2002\)128:8\(808\)](https://doi.org/10.1061/(ASCE)0733-9399(2002)128:8(808)).

847 Zhang, G., Wei, Z. & Ferrell, R.E., 2009. Elastic modulus and hardness of muscovite
848 and rectorite determined by nanoindentation. *Appl. Clay Sci.* 43, 271-281. doi:
849 <https://doi.org/10.1016/j.clay.2008.08.010>.

850 Zhang, G., Wei, Z., Ferrell, R.E., Guggenheim, S., Cygan, R.T. & Luo, J., 2010.
851 Evaluation of the elasticity normal to the basal plane of non-expandable 2:1 phyllosilicate
852 minerals by nanoindentation. *Am. Mineral.* 95, 863-869. doi:
853 <https://doi.org/10.2138/am.2010.3398>.

854 Zhou, B., Wang, J. & Wang, H., 2018. Three-dimensional sphericity, roundness and
855 fractal dimension of sand particles. *Géotechnique* 68, 18-30. doi:
856 <https://doi.org/10.1680/jgeot.16.P.207>.

857